UNIVERSITÉ DE GENÈVE
FACULTÉ DES SCIENCES

Delayed jet trigger at the LHC ATLAS for Run 3

Gentian Shatri

A thesis submitted in fulfillment of the requirements for the degree of Master of Physics

Supervisor: Prof. Anna Sfyrla

Département de Physique Nucléaire et Corpusculaire
Faculté de Physique
Université de Genève

June 24, 2022

Acknowledgements

First, I am extremely grateful to Prof. Anna Sfyrla who gave me the opportunity to pursue this thesis and from whom I learned a lot.

My sincere thanks to Dr. Claire Antel who gave me invaluable help throughout the year, especially regarding the Athena software.

I am grateful to Prof. Christian Ohm and Dr. Javier Montejo Berlingen, with whom we had very interesting discussions and to Dr. Chiara Rizzi who helped me at the early stages. Thanks also to Dr. Pantelis Kontaxakis who read and commented my thesis.

Lastly, I would like to acknowledge my parents and my brother, who supported me for five years.

Contents

List of Figures

List of Tables

List of Abbreviations

B	Baryon number
BT	Barrel Toroid
CS	Central Solenoid
DV	Displaced vertex
ECAL	Electromagnetic calorimeter
ECT	End-Cap Toroid
EW	Electroweak
HCAL	Hadronic calorimeter
ID	Inner Detector
IP	Interaction Point
L	Lepton number
LLP	Long-Lived Particle
LSP	Lightest Supersymmetric Particle
MSSM	Minimal Supersymmetric Standard Model
PV	Primary vertex
QCD	Quantum Chromodynamics
QED	Quantum Electrodynamics
QFT	Quantum Field Theory
SCT	Semiconductor Tracker
SM	Standard Model
SUSY	Supersymmetry
TRT	Transition Radiation Tracker

Introduction

In the twentieth century, physics in general has developed spectacularly. Two of the most exciting findings were first that matter can decay, and it is composed of newly discovered particles (neutrons, protons, and electrons) and second that it is possible to give a mathematical description of infinitesimal parts of nature with what is known today as quantum mechanics. But the latter, embodied by the Schrödinger equation, could not explain the behavior of relativistic particles. The union by Dirac in 1928 of the relativity with the quantum realm led to the discovery of the positron.

As the technological means started to develop at the same rate, high-energy accelerators and more sophisticated detectors that could probe smaller scales were designed. They allowed the measurement of a plethora of new *exotic* particles, never seen before.

Physicists desperately needed a framework who could provide a clear understanding of the building blocks of nature (if there are any) and could thus explain this *zoo* of particles.

They found it in a certain number of theories, grouped in what is called nowadays the Standard Model (SM). More so than understanding, this model predicts the existence of new particles. The last piece of the puzzle, the Higgs boson, was discovered by the ATLAS and CMS collaborations in 2012[1] and came to complete the model. Up to the day which this thesis is being written, no experiments have yet invalidated the Standard Model.

Nevertheless, there remain some phenomena that it fails to explain, such as the dark matter or the neutrino masses.

To overcome these deficiencies, beyond Standard Model (BSM) theories emerged. In these new models, particles with varied lifetimes arise. Via a mechanism like a small phase-space, these particles can acquire long-lifetimes such that they leave in the detector a *displacement* that can be measured.

However, the modern detectors are built for particles that decay promptly, meaning that the distance between their production point and the point at which they decay is smaller than the spatial resolution.

Those hypothetical particles have, theoretically, detector signatures that are different from the known ones and furthermore could look like typical noise. For example, a BSM long-lived particle (LLP) could provoke an anomalous ionization in the detector material or leave energy deposits without any track.

This could explain why none of these BSM particles were discovered because they require completely new processing and analyzing methods while current selection thresholds and triggers are not well suited for these cases and can even reject the BSM signals.

Numerous searches were performed, each exploiting one or more of these atypical signatures. Among them, some uses the fact that it is possible to reconstruct the point at which the particle decays. Although this type of analysis provides good sensitivity for LLPs created closed to the production point $\mathcal{O}(1-100\,\mathrm{mm})$, it becomes not viable for distances larger than that.

In this thesis, we use the timing as measured by the ATLAS calorimeter. What makes the calorimeter timing interesting is that the cells provide an offline time resolution below 1 ns. Heavy LLPs, by the relativistic momentum equation $p = \gamma m \beta$, have a smaller boost and thus move slowly through the detector. The jets produced as a result of the LLP decay will arrive later than the SM jets. At the present time, there is still no trigger to capture these specific delayed jets.

Thus, we propose here a feasibility study for such a trigger that could provide in the next stages of Run-III an interesting approach to BSM physics.

The thesis is organized in the following way:

- Chapter 2 is an extended version of the first paragraph of this introduction. The Standard Model and its limitations are briefly overviewed. It also gives a modest introduction to supersymmetry (SUSY) and in particular to split-SUSY.

- In chapter 3, the ATLAS detector and key concepts in the data processing chain are presented such as the distinction between online and offline reconstructed objects or how Monte-Carlo (MC) samples are generated.

- In chapter 4, we give a brief review of the long-lived particles' detector signatures. We also explain how the jet timing is determined in the calorimeter, and finally we summarize the CMS paper on delayed jets.

- In chapter 5, we study different trigger items and jet selections for different simulated R-hadron models (introduced in sect. 2.4). Moreover, we look at which cut in the maximum timing gives the best signal acceptance and an optimal background rejection.

- In chapter 6, after implementing the timing variable in the trigger software, we study the correlation between the online and offline jet timings.

Theoretical ground for long-lived particles

This chapter gives an overview of the elementary particles and the associated fundamental forces. It also extends the discussion to the limitations of this model and tries to provide a brief introduction to the next possible successful theory that goes beyond the SM : supersymmetry, which gives rise to particles with lifetimes usually greater than known particles.

2.1 The Standard Model

The theories developed by physicists to get a unified picture of nature are three. They are quantum field theories, meaning particles are described as local excitations of a corresponding field that permeates the whole universe. The forces between the fermions, particles with spin half an integer, are mediated by bosons, particles with spin an integer.

There are three of these QFT, describing each three of the four fundamental forces. The gravity, meanwhile, has no measurable effect at such a small scale and therefore no quantum field theory of gravitation exists yet.

THE ELECTROMAGNETIC FORCE

QED was first brought up to reconcile special relativity and quantum mechanics. It explains the electromagnetic interactions between charged particles. Each process can be represented, as in any QFT, by a Feynman diagram for which the amplitude can be calculated. Particles such as leptons (electron, muon, tau) interact by exchanging a photon; the strength of the interaction is given by the factor $\alpha \approx 1/137$. The leptons can also interact with antileptons (positron, anti-muon, anti-tau), which are leptons with only a reversed charge sign.

One of the experimental tests of QED was the measure of the Lamb Shift, which corresponds to a shift in atomic energy levels of the hydrogen atom and can be computed with the loop-level correction of an electron scattering a nucleus. It allowed physicists to determine with a precision of one in a million the value of the fine-structure constant.

THE STRONG FORCE

Then, allowing the photons to reach shorter wavelengths and so thus higher energies, the physicists were able to probe shorter distances and discovered that particles like hadrons were composed of more fundamental particles, called quarks. These were introduced first by theoreticians to explain the considerable number of baryons discovered.

There are six *flavors* of quarks (u, d, c, s, t, b). As leptons, they are charged, although of different magnitude, and of spin $1/2$ but behave differently in that they also subject to another force: the strong force, described by QCD, that confine them inside hadrons.

Indeed, the greater the distance between quarks, the greater the force. It is because they exchange gluons, which can interact with themselves forming gluon loops and resulting in a coupling strength increasing as the distance increases. In comparison, the QED coupling strength is about 100 times smaller than the QCD one with $\alpha_S \approx 1$.

Quarks and gluons have a unique property, which is they carry color. This property has been initially introduced to allow observed baryon states such as $\Delta^{++}(uuu)$ that are forbidden by the Pauli principle if the three quarks are not distinguishable. Color then has been demonstrated experimentally by electron-positron annihilation.

Quarks can have one of three colors : red, blue and green. Meanwhile, each gluon carries one color and one anti-color, giving eight states, therefore eight gluons exist. Colorless particles such as leptons and antileptons cannot *feel* the strong force.

THE WEAK FORCE

Many decays have been observed and some of them were considered to be evidence of the existence of a new force. For instance, it has been found that the pion can decay such as $\pi^- \to \mu^- \bar{\nu_\mu}$ with a lifetime 10^8 or 10^{15} greater than it would be expected if the force involved was electromagnetic or strong, respectively. Because the lifetime is inversely proportional to the coupling strength, this new force was called the weak force. This force was used to explain beta decays and is radically different from the other two because it does not conserve parity, meaning only left-handed fermion and right-handed antifermions can interact.

Furthermore, the reason the coupling is so low is that the boson mediating the force is very massive and then the propagator small. In fact, the coupling strength is $\alpha_W \approx 1/30$.

There are 2 types of weak interaction: the charged one involving a boson $W^\pm$, responsible for a change in flavor at the vertex and neutral one with a boson Z, which conserve flavor. Since all the particles possess a weak isospin, they all feel the weak force; neutrinos being massless and with no electric charge and no color, they only interact with matter by the weak force, explaining their very low cross-section.

QED and weak theory can be arranged together into what it's called the electroweak theory, described by the $SU(2) \times U(1)$ group. The spontaneous symmetry breaking of the EW theory gives rise to the gauge bosons W, Z and γ and via the Higgs mechanism confers them a mass. So to say, gauge bosons acquire a mass by interacting with the Higgs boson of spin zero.

Tab.2.1 summarizes some properties of the elementary particles of the Standard Model.

No model is perfect. The next section focuses on reviewing the various aspects of nature that the SM can't explain.

	Particle	Q/e	M [GeV]	Force/Coupling
LEPTONS ($S = \frac{1}{2}$)	e^-	-1	$5 \cdot 10^{-4}$	E, W
	ν_e	0	$< 10^{-9}$	W
	μ^-	-1	0.106	E, W
	ν_μ	0	$< 10^{-9}$	W
	τ^-	-1	1.78	E, W
	ν_τ	0	$< 10^{-9}$	W
QUARKS ($S = \frac{1}{2}$)	d	-1/3	0.003	E, W, S
	u	2/3	0.005	E, W, S
	s	-1/3	0.1	E, W, S
	c	2/3	1.3	E, W, S
	b	-1/3	4.5	E, W, S
	t	2/3	174	E, W, S
GAUGE BOSONS ($S = 1$)	γ	0	0	EW, 1/137
	8 gluons	0	0	S, 1
	$W^\pm$	± 1	80.4	EW, 1/30
	Z	0	91.2	EW, 1/30
HIGGS BOSON ($S = 0$)	H	0	125	Yukawa, $\propto m_p$

TABLE 2.1: Elementary particles of the SM and their charge, mass, and the forces exerted on them in case of the fermions and the coupling strength for gauge bosons. The Higgs boson couples with a particle via a Yukawa interaction, and the strength is proportional to that particle's mass. The masses were taken from Ref. [2]

2.2 The limits of the Standard Model

The goal here is to show why the SM is incomplete and that some discrepancies, that are still not resolved, can be settled by supersymmetry.

THE HIERARCHY PROBLEM

One of the problems that was first identified is related to the loop corrections to the Higgs propagator, and more specifically to the corrections of m_H^2 by virtual particles that couple with the Higgs field. Indeed, going to a very large scale such as the Planck scale ($\approx 10^{19}$ GeV), these quantum corrections become much bigger than the mass of the Higgs itself.

One can illustrate this by looking at corrections from a fermionic loop and bosonic loop, as shown in Fig. 2.1 ([3]).

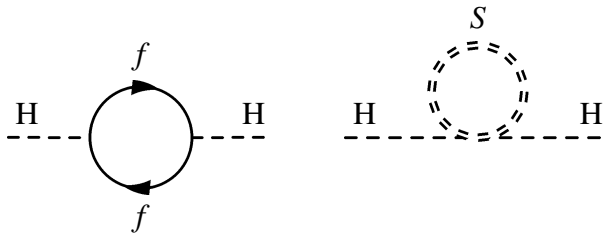

FIGURE 2.1: Feynman diagrams of two possible loop corrections to the Higgs propagator

Let's assume the Lagrangian has two terms : one that couples the Higgs field to the fermion (any leptons or quarks in the SM) with $-\lambda_f H f \bar{f}$ and the other describing the coupling between some heavy scalar S of mass m_S via $-\lambda_S \mid S \mid^2 \mid H \mid^2$.

The correction to the Higgs mass is then :

$$\Delta m_H^2 = -\underbrace{\frac{\mid \lambda_f \mid^2}{8\pi^2}\Lambda_{UV}^2}_{Dirac} + \underbrace{\frac{\lambda_S}{16\pi^2}[\Lambda_{UV}^2 - 2m_S^2 \ln(\Lambda_{UV}/m_S)]}_{Scalar} \tag{2.1}$$

First, we see that because of the presence of the UV-cutoff Λ_{UV} in the Dirac term, the mass of all particles depends quadratically on the mass-scale. Moreover, in the case of the scalar term, there is also a quadratic dependence on the mass of the heavy scalar.

Fortunately, looking more carefully, we can see a minus sign, indicating that the two contributions may cancel out. Indeed, if each Dirac fermion come in pair with two complex scalars with $\lambda_S = \mid \lambda_f \mid^2$, then the UV terms will disappear. If we assume that fermions and bosons are symmetrically related, then the scalar masses are also cancelled. Therefore, this relation, called supersymmetry, provides a cure for this problem. More on that in section 2.3.

THE COLD DARK MATTER

As astronomers started observing the galaxies, they looked at the velocity distributions of star's orbits around the galaxy center. From the Newton law of gravitation, we would expect v having a $r^{-1/2}$ dependence. Instead, the velocity, for objects far from the center, was constant, which suggests a linear relation between mass and radius. Physicists at that time concluded that a dark component is involved in the total mass of the galaxy.

Nowadays, the ΛCDM model describe the total energy-matter density with a parameter Ω. According to this model, the Universe is made of 5% of ordinary or baryonic matter ($\Omega_B \approx 0.05$), 23% of cold dark matter or CDM ($\Omega_C \approx 0.23$) and finally 72% of dark energy ($\Omega_\Lambda \approx 0.72$).

This model also suggests that CDM is composed of weakly interacting particles with masses in the TeV range. A potential candidate is the lightest supersymmetric particle (LSP) predicted, as its name suggest, by supersymmetry, which is introduced in the next section. The idea is that, as the Universe cools after the Big Bang, the heavy particles will decay, so that only light particles such as photons, neutrinos, electrons, LSPs, u and d quarks remain. At the beginning, superpartners were also there but became progressively LSPs. The energy density of the latter can be computed using different models and ends up being very close to the CDM density, confirming that supersymmetry might be an explanation[4].

OTHER MYSTERIES

We shortly introduced what we think are the two major problems that supersymmetry can solve. There are of course many more, related to SUSY.

For instance, supersymmetry explains in some way the breaking of the electroweak symmetry. Also, by looking at coupling strengths dependencies on energy, it is possible to show that the three forces meet at an energy around 10^{16} GeV : supersymmetry describe a good unification at that scale. Finally, there is the matter/antimatter asymmetry problem, which states that there must be some mechanisms happening in the early Universe that justify a complete absence of anti-baryons in the Universe : multiple hypothesis, which require SUSY to a certain extent, have been made to explain it.

In conclusion, the Standard Model although being a very well experimentally verified theory explaining a lot of phenomena occurring in Nature, is only valid at energy scale of 100 GeV and is unable to account for important observations. That is why many physicists argued a need to extend the SM and developed many theories to do so, like supersymmetry, which is seen as the best candidate.

2.3 Supersymmetry

In this section, we focus on briefly introducing the theory of supersymmetry and the reasons for the prediction of the long-lived particles. Inside this framework, there are many models, but we will in particular present one that is of interest to us : the split supersymmetry.

Almost all the information that appear in this section was taken from [5].

2.3.1 General considerations

A supersymmetry operator Q can be defined such as:

$$Q\,|F\rangle = |B\rangle\,, Q\,|B\rangle = |F\rangle \tag{2.2}$$

This is an operator that turns a fermion into a boson and a boson into a fermion. A quick look at these two equalities indicates that $Q^{\dagger}$ is also a symmetry generator. These two operators have a spin of $1/2$, making therefore supersymmetry also a spacetime symmetry.

Single-particle states for this QFT are called *supermultiplets*. Each of these have an equal number of fermion and boson degrees of freedom, i.e. $n_B = n_F$. Fermions and bosons inside a supermultiplet are *superpartners*. Particles falling in the same supermultiplet have equal masses.

Every supermultiplet with $n_B = n_F$ can be constructed from a combination of *chiral* supermultiplets and *gauge* supermultiplets :

- Chiral : a two-component Weyl fermion (massless $S = 1/2$ particle) and two real scalars or one complex scalar (spin $S = 0$). Because a Weyl spinor has two possible helicity states, then $n_F = 2$. And obviously, $n_B = 2$

- Gauge : with the requirement of a renormalizable theory, we can take a massless spin-1 boson for which there are two possible helicity states ($n_B = 2$) and therefore that need to be associated with a Weyl fermion, so that $n_F = 2$.

We must be able to construct chiral supermultiplets with quarks, leptons and Higgs bosons while photons, gluons, and bosons W,Z must fit into the gauge supermultiplets.

We need two Higgs supermultiplets with each one a hypercharge $Y = \pm 1/2$, so that gauge anomalies cancel and that these supermultiplets give masses to up-type and down-type quarks via the Yukawa coupling. The complex scalar field for $Y = 1/2$ is H_u and the one for $Y = -1/2$ is H_d. The components for H_u and H_d are $(H_u^+ H_u^0)$ and $(H_d^0 H_d^-)$ respectively. The superpartners are two charged and two neutral Weyl fermions.

For gauge bosons, we must take the one before EW symmetry breaking, i.e $W^\pm$,W^0 and B^0.

To distinguish between superpartners of fermions and those of bosons, a specific terminology is used. Indeed, since Weyl fermions are associated with scalars, we add an "s" before the name of the fermion. For instance, the superpartner of an electron is a **s**electron.

The name of the boson's superpartner is constructed by adding an "ino" at the end. The gluon's superpartner is then the glu**ino**. We write superpartners by adding a tilde over the SM particle letter : $\tilde{e}, \tilde{g}$.

The gauge bosons are called wino and bino, and they mix to give the zino ($\tilde{Z}$) and the photino ($\tilde{\gamma}$).

Tables 2.2,2.3, and 2.4 summarize the different supermultiplets.

name/sname	$S = 1/2$	$S = 0$
fermion/sfermion	$(u_L\ d_L)$ $(u\ e_L)$	$(\tilde{u_L}\ \tilde{d_L})$ $(\tilde{u}\ \tilde{e_L})$
$\bar{f}$	$f_R^\dagger$	$\tilde{f}_R^*$

TABLE 2.2: Chiral supermultiplets for one family of leptons and quarks. The second line represent the singlet supermultiplet for an antifermion.

higgsinos/higgs	$S = 1/2$	$S = 0$
H_u	$(\tilde{H_u^+}\ \tilde{H_u^0})$	$(H_u^+\ H_u^0)$
H_d	$(\tilde{H_d^0}\ \tilde{H_d^-})$	$(H_d^0\ H_d^-)$

TABLE 2.3: Higgs double supermultiplets.

name/namino	$S = 1$	$S = 1/2$
gluon, gluino	g	$\tilde{g}$
W, wino	$W^\pm, W^0$	$\tilde{W}^\pm, \tilde{W}^0$
B, bino	B^0	$\tilde{B}^0$

TABLE 2.4: Gauge supermultiplets.

One problem arises : if SUSY was truly an exact symmetry, then we would have observed a long time ago particles with the same mass as the SM particles but with different spin. It means supersymmetry is broken.

The reason these particles have not been discovered yet is because of their heavy mass (which we clarify below). Indeed, because the mass of the SM particles depends on the EW symmetry breaking, then their mass should be bounded by the top by the vacuum expectation value, i.e. 246 GeV. Instead, the superpartners don't need this to have a mass, meaning they can be as heavy as they want.

For SUSY to solve the hierarchy problem after symmetry breaking, the latter must be soft such that the Lagrangian is the sum of two parts, namely the $\mathscr{L}_{\mathscr{O}}$ that preserves SUSY and that describes the Yukawa couplings and contains dimensionless scalar couplings, and the $\mathscr{L}_{\mathscr{S}}$, which corresponds to the soft symmetry breaking term and have all the couplings with positive mass dimension and the mass terms.

The correction to the Higgs's mass is :

$$\Delta m_H^2 = m_S^2\left(\frac{\lambda}{16\pi^2}\ln\frac{\Lambda_{UV}}{m_S} + \cdots\right) \tag{2.3}$$

Where m_S is the largest mass in $\mathscr{L}_{\mathscr{S}}$. Since Δm_H^2 is proportional to m_S, then the latter should not be too large because it would completely obliterate the chances to address the hierarchy problem. Thus, to have a VEV that gives the W and Z bosons their mass, m_S should be around 1 TeV.

What we have described here in the most general way is called the minimal supersymmetric standard model (MSSM). For completeness, we can show the superpotential associated to this model[6] :

$$\begin{aligned} W = &[\lambda_u^{ij} Q^i H_u \bar{U}^j + \lambda_d^{ij} Q^i H_d \bar{D}^j + \lambda_e^{ij} L^i H_d \bar{E}^j + \mu H_u H_d] \\ &+ [\alpha_1^{ijk} Q^i L^j \bar{D}^k + \alpha_2^{ijk} L^i L^j \bar{E}^k + \alpha_3^i L^i H_d + \alpha_4^{ijk} \bar{D}^i \bar{D}^j \bar{U}^k] \end{aligned} \tag{2.4}$$

with the fields $L = (\nu \quad e)_L$, $Q = (u \quad d)_L$, $\bar{E} = e_R^\dagger$, $\bar{U} = u_R^\dagger$, $\bar{D} = d_R^\dagger$ and where the indices i, j run from 1 to 3.

The first term corresponds to the SUSY extension of the Yukawa couplings. The second term can be brought to generalize the superpotential, but it has the peculiarity to not conserve the baryon and lepton number. If the conservation of B and L was not true, then we would have observed a proton decay via $p \to e^+\pi^0$. But this is not yet the case.

To remedy this, one must require R-parity (also called matter parity) conservation to forbid baryon and lepton number violation. This discrete symmetry is defined by the operator :

$$P_R = (-1)^{3(B-L)+2S} \to \begin{cases} P_R\,|SM \quad particles\rangle = |SM \quad particles\rangle \\ P_R\,|superpartner\rangle = -\,|superpartner\rangle \end{cases} \tag{2.5}$$

It is positive for ordinary particles and negative for superpartners. Therefore, superpartners are produced in pairs and the LSP, if we assume R-parity is conserved, can not decay to a lighter particle with negative R-parity, and thus it must be stable.

If the LSP is neutral then it interacts feebly, so it is a possible candidate for cold dark matter as previously explained.

In SUSY, the LSP is called the lightest neutralino ($\tilde{\chi}_1^0$). In fact, this particle arises from the mixing of the bino, the neutral wino and the neutral higgsinos.

2.3.2 Supersymmetric particle decays

For a particle of mass m_A that decays such as $A \to 1+2+\cdots n$, the lifetime can be calculated theoretically using basic QFT :

$$\tau = \frac{2m_A}{\int \mid \mathscr{M} \mid^2 d\phi^{(n)}} \tag{2.6}$$

where $\mathscr{M}$ is the amplitude of the decay process and $d\phi^{(n)}$, the phase-space of the final products.

If the phase-space or the amplitude are small, τ can be big. The first can occur if the particle can not decay due to a symmetry, as it is the case for the LSP. The second factor would be that the decay happens at a scale much larger than m_A.

Therefore, MSSM (or in fact any SUSY related model) can predict long-lived particles. We propose here to show some of these particle decays and the different possible signals they can give rise to. A more extensive overview of the detector signatures is done in chapter 4.1.

Since the *irreducible* particle is the LSP, all the SUSY particles will chain decay until a $\tilde{\chi}_1^0$ is produced. The thing to look for is missing transverse momentum or energy (E_T^M).

SLEPTON

The decay of the slepton depends on the nature of the LSP. More specifically, if the lightest neutralino is more bino-like (deep gaugino region), then the right-handed sleptons will tend to decay to the LSP and leptons such as $\tilde{l}^{\pm} \to l^{\pm}\chi_i^0$ (figure 2.2). In the detector, this occurs as two charged leptons (obviously) with missing transverse momentum.

The left-handed slepton are more higgsino like (higgsino region), therefore they will decay the second neutralino or charged neutralinos.

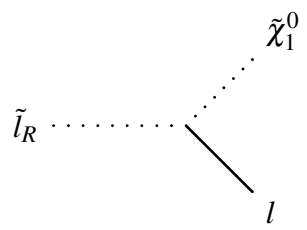

FIGURE 2.2: Feynman diagram for a right-handed slepton decay in the gaugino region.

SQUARK

Two types of decays are possible. The first corresponds to a production of a quark and gluino. If the latter is lighter than the squark, then the vertex has a

strong coupling, meaning the squark can decay via QCD (figure 2.3). Otherwise, the right-handed and left-handed squarks decays the same way as the L-sleptons and R-sleptons.

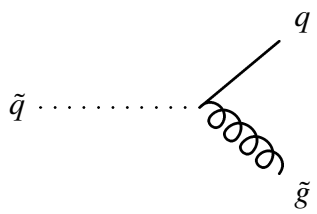

FIGURE 2.3: Feynman diagram the QCD decay of the squark.

GLUINO

The gluino generally decays in cascades. If it is heavier than a squark, then it can produce an antiquark and a squark, which decays into a quark and the lightest neutralino. It manifests as two jets and missing E_T as shown in figure 2.4.

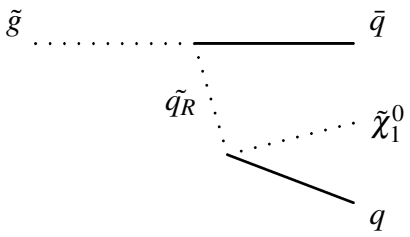

FIGURE 2.4: Feynman diagram for a gluino decaying into two jets.

Otherwise, if the gluino is lighter than the squark, its decay is mediated by the weak force producing charginos, jets and leptons.

Finally, the gluino's decay can also produce b-jets.

In conclusion, we have presented what is the minimal supersymmetric model, and we showed the different particles that are predicted. In the next section, we give a short introduction to split SUSY, a SUSY related model, which we use as a benchmark to perform our studies.

2.4 Split supersymmetry

This new model ([7]) no longer focuses on the hierarchy problem but states that nature is finely tuned. It is possible then to choose a high-energy scale for symmetry breaking, typically at $m_S \gg 1000$ TeV.

Therefore, the scalars are very heavy, meanwhile the Higgs's mass is either acquired by some mechanism or it is finely tuned. The fermions are much lighter, like for example the gluino. The new SUSY mass spectrum is divided in these two categories, hence the name split SUSY.

The heavy scalars prevent flavor changing interactions while the light fermions assure a dark matter candidate, the lightest neutralino (same as before).

The gluino can decay only to a very heavy squark, meaning the decay is suppressed by the energy scale at which symmetry breaking happens.

One can show that the gluino's lifetime goes like:

$$\tau \propto \frac{m_S^4}{m_{\tilde{g}}^5} \tag{2.7}$$

For an energy scale of 1 TeV, the gluino has a lifetime big enough such that it will hadronize to a composite particle called the R-hadron, because it has one unit of R-parity.

It comes in three types : the R-meson ($g\tilde{q}\bar{q}$), the R-baryon ($\tilde{g}qqq$)) and the R-gluon ($\tilde{g}g$). Generally, the fragmentation probability into a charged or neutral R-hadron should be the same[8].

For higher scales, the gluino will decay at the outer edge of the detector. At a scale of 10^{13} GeV, the gluino become stable.

A possible process that can produce a long-lived gluino is the one pictured in the figure 2.5. The gluino decays first to a quark and squark. The latter is highly virtual and thus the gluino is long-lived. It then decays to a quark and the lightest neutralino $\tilde{\chi}_1^0$. Because $\tau_{\tilde{g}}$ is much bigger than the hadronization timescale, an R-hadron will be produced.

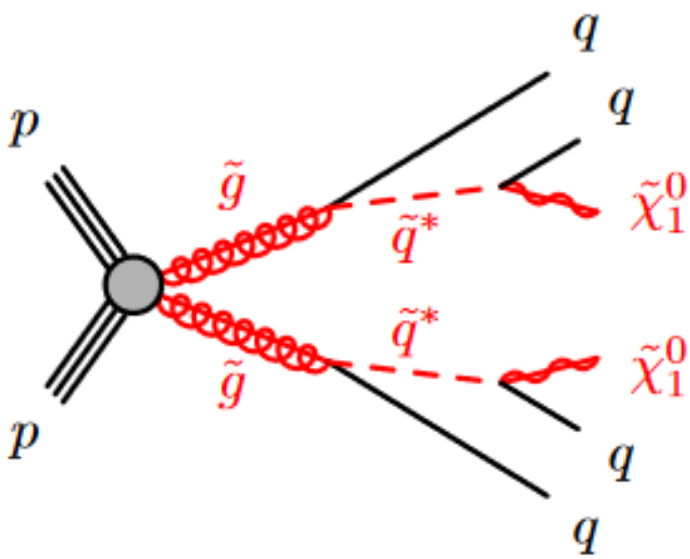

FIGURE 2.5: Feynman diagram corresponding to a production of long-lived gluino decaying to two quarks and a $\tilde{\chi}_1^0$.

The ATLAS detector

The Large Hadron Collider (LHC), situated under the French-Swiss border, is the biggest particle accelerator in the world and is considered to be the largest current scientific experiment. It was built by the European Organization of Nuclear Research (CERN) and started operating on 10 September 2008.

It consists of a circular ring with a circumference of 27 km with accelerating infrastructures. Inside, two protons beams collide, with a center-of-mass energy of 14 TeV, every 25 ns and with a luminosity $L = 1 \times 10^{34}\,\mathrm{cm}^2\,\mathrm{s}^{-1}$. The terminology will be explained in the next section.

Multipurpose detectors are placed at different points on the circular ring to unravel new physics, as shown in the figure 3.1 below. There are four of them. CMS (compact muon solenoid)[9] for instance probe SM particles and looks for BSM particles. Another one, ALICE (A Large Ion Collider experiment)[10] focuses on studying heavy-ion physics. The third detector is LHCb (Large Hadron Collider Beauty)[11], which looks for matter-antimatter differences through the study of the b-quark.

In this chapter, we focus on presenting the last one, which is called *A Toroidal LHC ApparatuS* or ATLAS. The research at ATLAS is close to the one at CMS, however the design of the experiment and the investigating techniques are different.

We will describe in a very general manner some of its characteristics. Most information can be found in [12], [13].

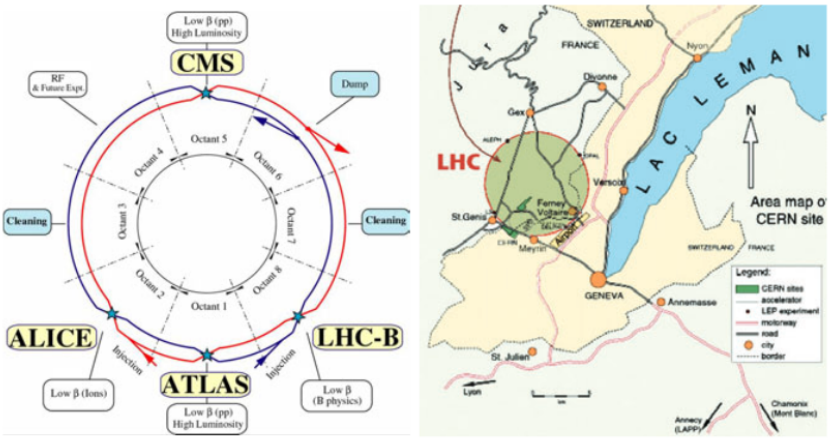

FIGURE 3.1: (LEFT) Configuration of the LHC and position of the detectors. (RIGHT) Geographic location. Taken from [14, p. 30].

3.1 General concepts

Before diving into the experimental apparatus, it is frequent practice to expose the nomenclature and physics concepts used in collider physics.

An important quantity, which is recurring in all papers related to high-energy physics is the center-of-mass (CM) energy. It is defined to be $\sqrt{s}$ i.e. the square root of the Mandelstam variable s in the CM frame where the sum of the momentum $\vec{p}_i$ of all particles involved is 0. For the specific case of a two particle collision[1]:

$$s = \sum_{i=1}^{N} E_i^2 - \sum_{i=1}^{N} \vec{p}_i{}^2 = (E_1^{CM} + E_2^{CM})^2 \tag{3.1}$$

where E_i^{CM} is the energy of the particle i in the CM frame. Using the invariance of s, it is possible to express these CM energies as a function of the energies and the momenta in the laboratory frame. The energy available (s) will be greater for two colliding beams than a colliding particle and a mass at rest. Thus, colliders like LHC provide a good way to probe more fundamental processes.

Another widely used quantity is the total luminosity. For a more intuitive understanding, it can be linked to the number of events N of a given process with cross-section σ (likelihood of that process) and counted in a given time. The formula is the following one :

$$N = \sigma \cdot \int dt \mathscr{L}(t) \tag{3.2}$$

Here $\mathscr{L}(t)$ is called the instantaneous luminosity and when integrated over time gives the total luminosity L. When two beams of particles with a 2D Gaussian profile and with a number of particles N_1 and N_2 in each, collide at a frequency ν :

$$\mathscr{L} = \nu \frac{N_1 N_2 N_b}{4\pi\sigma_x\sigma_y} \tag{3.3}$$

Where N_b is the number of bunches and σ_x and σ_y are the root-mean-square beam sizes. The factor 4π comes from the integration over the $X-Y$ plane.

The beam axis is the Z-axis and the transverse plane is therefore the plane $X-Y$. The X-axis points from the interaction point (IP) to the center of the LHC ring, and the Y-axis is simply pointing up.

Two angles then can be defined : θ is the one in the $X-Z$ plane, and ϕ is the angle in the $X-Y$ plane.

The first angle is used to compute the angle of the jets relative to the beam axis and is incorporated in the pseudorapidity as $\eta = -\ln(\tan\theta/2)$. This quantity is useful because $\Delta\eta = \Delta\eta'$ i.e. the difference in pseudorapidity is invariant under a boost along Z.

The second angle measure the distance from the beam in the transverse plane and is used a lot with other variables such as p_T or E_T^{miss}. These variables are of particular interest since they determine quantitatively the invisible contribution from feebly interacting particles. Indeed, because the momentum is conserved, p_T must

[1] With the natural units $\hbar = c = 1$

be equal to 0 before and after the head-on collision. If the final momentum in the transverse plane is not null, then some particle's momenta is missing.

The missing transverse energy/momentum quantify this absence and is defined as the sum over visible states:

$$E_T^{miss} = -\sum_i \vec{p}_i^T \tag{3.4}$$

Finally, another largely used quantity is the distance in the η-ϕ space, i.e.

$$\Delta R = \sqrt{(\Delta\eta)^2 + (\Delta\phi)^2} \tag{3.5}$$

3.2 Overview of ATLAS

ATLAS is able to identify most of the charged and very energetic particles like electrons, photons and jets thanks to electromagnetic and hadronic calorimeters. Moreover, it can reconstruct the tracks of these particles coming from the IP, enabling the measurement of the momenta, in association with a magnet system that bends the particle's trajectory.

At the outer edge, a muon system is capable to realize, with high precision, measurement of very energetic muons. Finally, an important part is the triggering, which must be very efficient in order to allow the detection of interesting physics.

This detector must be able to operate at a luminosity of $1 \times 10^{34}\,\mathrm{cm}^2\,\mathrm{s}^{-1}$. The uniform magnetic field needed dictates the shape of the whole detector. Indeed, it could have been an assembly of concentric spherical shells, but instead it is a more of a cylinder. ATLAS is $44m$ long, has a radius of 25 m and weights 7000 t.

In the figure below can be found a schematic diagram of the detector and its dimensions.

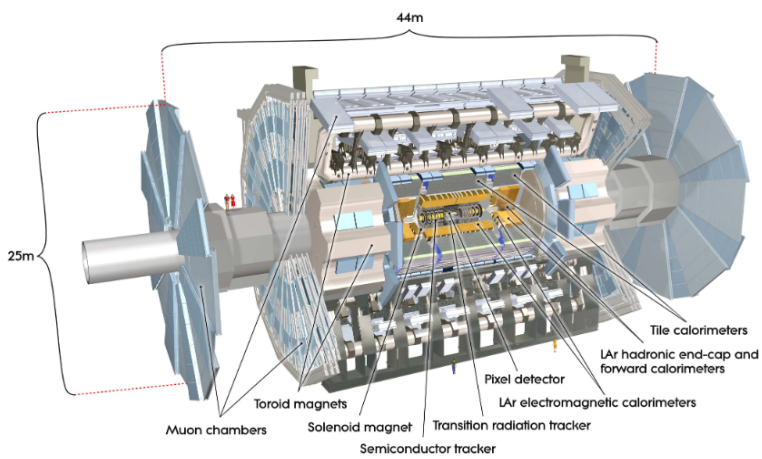

FIGURE 3.2: Schematic overview of the ATLAS detector.

3.3 Magnet system

There are two parts that serve different purposes. Both are made of superconducting material, cooled down to a temperature around 4.5 K by a cryogenic system.

First, the central solenoid (CS), which is concentric with the beam, provides the inner tracker with a magnetic field of 2 T, thus allowing the measurement of the momenta by studying the bending of the track. Because the CS is in front of the electromagnetic calorimeter (ECAL), one must minimize the amount of material to keep the radiative thickness as low as possible. It is done by using a single-layer coil wound by aluminum stabilized niobium-titanium (NbTi). This material is used because it is an alloy, and thus it is easy to produce and cheap. The intensity of the current flowing in the superconducting wires is 8 kA.

Then, there are the barrel toroid (BT) and two end-caps toroids (ECT) that are also arranged symmetrically around the beam. The ECT is rotated by some angle with respect to the BT in order to improve the bending. The three toroids are made of eight coils, both with a winding of Al-stabilized NbTiCu. The sixteen coils of the two ECT and the eight coils of the BT are connected in series, and are powered by a current of 21 kA. These two structures provide a magnetic field for the muon system of 0.5 T (BT) in the central region and of $1T$ (2 ECT) in the end-cap regions.

The figure 3.3 below shows the magnetic winding of the BT and ECT and the tile calorimeter steel. The CS winding is located inside the calorimeter.

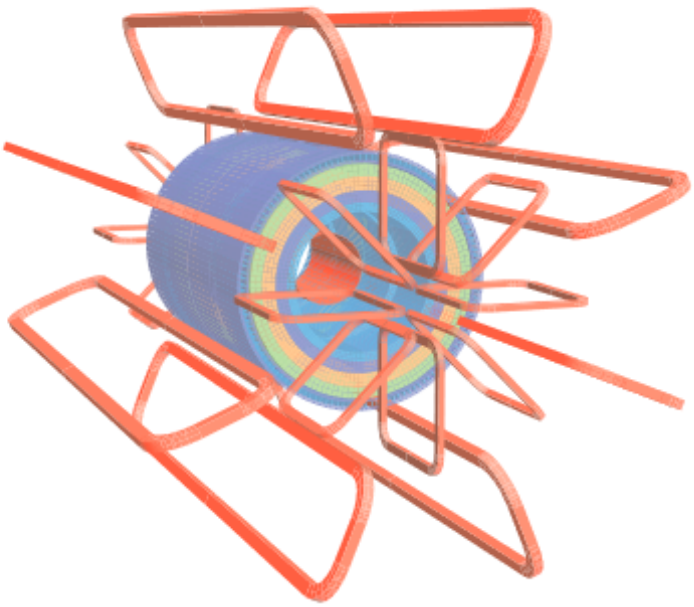

FIGURE 3.3: Schematic diagram of the winding of the ATLAS detector, for both the barrel toroid and the end-cap toroids. The central solenoid winding is inside the calorimeter.

3.4 Tracking technology

Since the beam crossing happen every 25 ns, there are a lot of tracks that need to be sorted out such that momenta and positions of the vertices can be extracted. The detector then must have high momentum resolution and must be able to distinguish with precision primary and secondary vertices. The inner detector (ID) is subjected to 2 T magnetic field that bend the particle trajectories and that are then synthesized by three layers of detecting material, as shown in figure 3.4. The first two, the pixel and the semiconductor tracker (SCT) allow high granularity and the outermost one, the transition radiation tracker (TRT) provide the detection of numerous tracks.

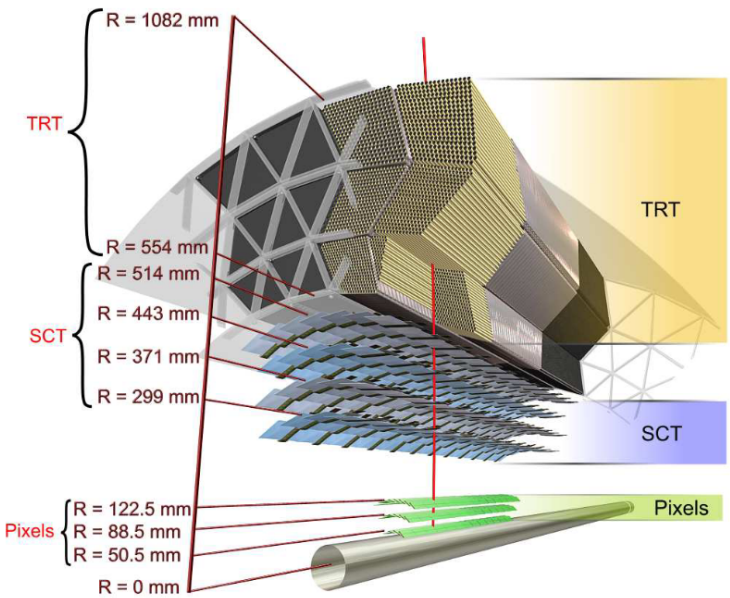

FIGURE 3.4: Schematic cross-section of the inner tracker. The red line is a charged particle track with a p_T of 10 GeV.

The region around the IP being the most exposed zone of the detector to radiation must be robust to aging effects. Overall, there need to be a compromise between materials with cost as low as possible and efficiency. We present below the distinct parts of the ID.

PIXEL DETECTOR

The pixel detector is placed where the flux of particles is the highest. More specifically, this detector is a silicon pixel one with cell of sizes $50 \times 400\,\mu m^2$. There are three of them at radii of 5, 9, and 13 cm. This region provides a very good measurement of the position and covers an area of $80\,m^2$ with 80 million readout channels. Usually, a track creates three hits.

SEMICONDUCTOR TRACKER

The SCT is situated in the middle region of the ID, at about 30 cm. It allows a measurement of the momentum and is generally associated with eight hits. There are eight layers of silicon microstrip detectors. The strips are placed at an angle of 40 mrad with respect to the Z-axis to determine the z coordinate.

Tracks can be sorted only if their separation is about 200 µm. The detector is composed of 61 m^2 of these silicon detectors with a total of 6 million readout channels.

TRANSITION RADIATION TRACKER

The TRT is an assemblage of 300,000 straw tubes filled with xenon gas and allows the measurement of about 36 tracking points per track. Furthermore, it can provide a continuous tracking and is also capable of identifying electrons because it assures a pion rejection factor between 20 and 100 for particles with a p_T of 20 GeV. There are approximately 350,000 readout channels.

3.5 Calorimetry

ATLAS uses two calorimeters to measure the energy deposited by particles like electrons or photons and hadronic jets. The important feature is that it must be able to differentiate between the two contributions.

THE ELECTROMAGNETIC CALORIMETER

The first calorimeter, the electromagnetic calorimeter, measures with good resolution the energy and the position of electrons and photons. There are two parts : a barrel one that covers $|\eta| < 1.475$ and two end-caps with a coverage of $1.375 < |\eta| < 3.2$.

The ECAL structure is similar to that of an accordion. Indeed, there are lead layers that create the electromagnetic shower and they are separated by regions with liquid argon that measure the energy deposited.

Moreover, the total length of the detector must be adjusted so that showers are contained fully in the material. Therefore, the ECAL is 22 radiation lengths. The required energy resolution [13] for the ECAL is:

$$\frac{\sigma_E}{E} = \frac{10\%}{\sqrt{E}} \bigoplus 0.7\%$$

The timing resolution at large energy deposits, on the other hand, is around 250 ps for high gain and 300 ps for medium gain[15]. For low energy deposits, the resolution becomes worse for high gains.

THE HADRONIC CALORIMETER

The second calorimeter, the hadronic calorimeter (HCAL), has full coverage and determine with precision the energy of the jets. There are three distinct sections in the HCAL that provide a covering range of $|\eta| < 4.9$.

The tile calorimeter is made of scintillating tiles embedded in iron. The light from the two side of one tile is directed with wavelength shifting fibers to two photomultipliers. It is placed behind the ECAL and is divided in the azimuthal direction in 64 modules.

Then for pseudorapidites of three and higher, liquid argon is used both in hadronic end-cap calorimeter and in the forward calorimeter. The two are contained in the same cryostat that includes also the electromagnetic end-caps.

For the HCAL, the energy resolutions go like :

$$\frac{\sigma_E}{E} = \frac{50\%}{\sqrt{E}} \bigoplus 3\% \quad \text{(barrel and end-cap)}$$
$$\frac{\sigma_E}{E} = \frac{100\%}{\sqrt{E}} \bigoplus 10\% \quad \text{(forward)}$$

The timing resolution at high energy is 162 ps at high gain and 262 ps at low gain.

The figure 3.5 shows an illustration of the calorimetry system and where the different parts are located.

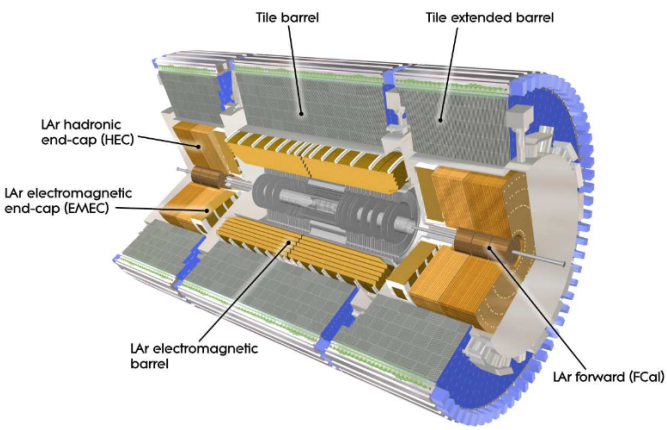

FIGURE 3.5: Schematic diagram of the different sections of the calorimetric detector.

3.6 Muon system

The muon spectrometer (MS) is an assemblage of different chambers that serve two purposes. The first corresponds to the measurement of the muon tracks that are bend by the toroid magnets, as explained in section 3.3. The second is the triggering of the muons.

The chambers are placed in cylindrical layers around the beam pipe and therefore needs to be carefully aligned.

First, monitored drift tubes provide with the determination of the trajectories in association with the ID. When the pseudorapidity increases, cathode-strip chambers are used.

For $|\eta| < 2.4$, resistive plate chambers in the barrel and thin gap chambers in the end caps allow the measuring of a second coordinate orthogonal to the one determined by the previous chambers and the identification of bunch crossings. The figure 3.6 shows the different sections of the MS.

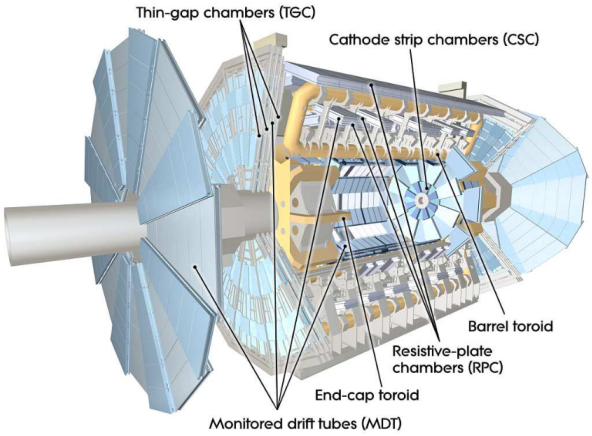

FIGURE 3.6: Schematic diagram of the ATLAS detector with the different parts of the muon spectrometer indicated.

3.7 Trigger architecture and DAQ system

The event rate when the two beams collide is approximately 40 MHz, which is too big to be correctly treated.

This is the reason why selections need to be applied in order to reduce it to 100 Hz while still keeping good data to be stored and then analyzed.

These tasks are performed by the trigger system.

A diagram of the trigger and data acquisition system is displayed in figure 3.7:

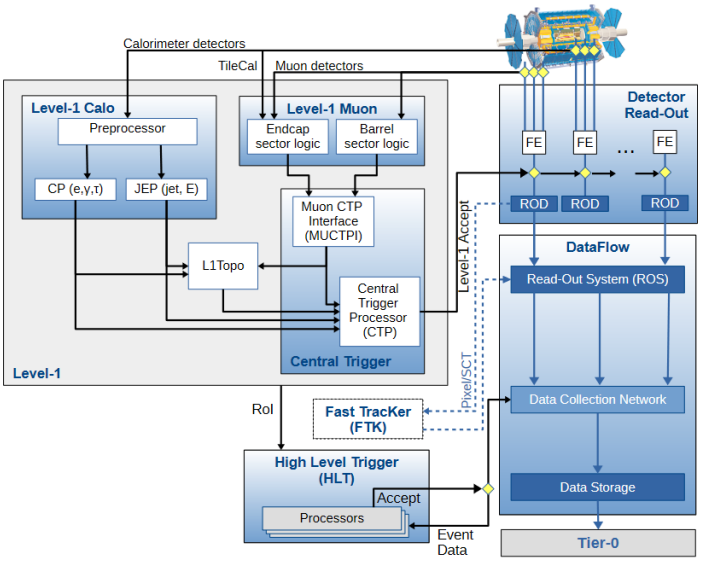

FIGURE 3.7: The ATLAS TDAQ system[16].

In the first place, the Level-1 or L1 trigger system selects the data coming from the detectors.

For instance, the L1Calo takes information from the calorimeters and sends it in digitized and calibrated form to the cluster processor and the jet/energy sum processor. The first looks for charged leptons (e, τ) and photons that have a transverse momentum above some threshold. The second searches for objects like jets and determine their missing transverse energy for example.

The L1Muon uses the data from the MS's trigger chambers in the barrel and in the end-caps to look for muons with high p_T.

The information coming from the L1Calo and L1Muon are then fed to the central trigger processor (CTP). Before entering the CTP, the data is combined into topological algorithms. After that, the CTP creates a trigger menu with 256 items from a combination of the multiple selections applied. More on that in section 3.7.1.

CTP plays an important role because it applies a dead time that is calculated to limit the effects of two times. One of them is the simple dead time, which corresponds to the time limit between two L1 accepts. The other, the complex dead time is the limit number of L1 accepts in multiple bunch crossings. Therefore, it is crucial to stake out each bunch crossing : in the case of the calorimeter trigger, it is more difficult because the signal pulse shape spans on several bunch crossings.

In summary, the L1 is a system of hardware processors that accepts events at a rate of 100 kHz and the time between a collision and the trigger decision (latency) is 2.5 µs.

The L1 accepted event is then sent to the Front-End detector electronics. The readout drivers (ROD) process the data and the readout system (ROS) buffer it. Indeed, for a single bunch crossing, the data is held by the ROS until the next trigger level, the high level trigger (HLT), makes a decision. In addition to the previous selections, the HLT uses also coordinates (η-ϕ plane) of regions of interest (ROI) that were determined by the L1 trigger.

Contrary to L1, the HLT perform fast selections using CPU-farms and is software based. The HLT can utilize all the data collected by the L1, but it focuses primarily on the information stored in the ROS that coincide with the ROI. The whole process ends by applying a hypothesis algorithm that decides whether the trigger decision was verified or not. The event rates drops to about 1.2 kHz. An event that is accepted by HLT is permanently stored in the Tier-0 facility and thereafter reconstructed offline and *processed*.

3.7.1 Trigger menu and items

The trigger menu lists the triggers at L1 and HLT. Indeed, a total of 512 L1 items and 1500 HLT chains are used[17].

Item here implies a trigger name that specifies a kinematic selection at one trigger level and for a certain type of physics object. For example, `L1_XE50` means $E_T^{miss} >$ 50 GeV at the L1. `HLT_mu20` refers to at least one muon with $p_T > 20$ GeV at the HLT. For the latter, the particle type letter (j for jet, e for electron, ...) is written in the lower case while it is written in the upper case for L1.

A chain is an L1 item followed by a sequence of HLT algorithms.

The L1 and HLT triggers have generally a prescale value $p_{L1,HLT} \geq 1$ that limits the number of accepted events by each trigger level. When $p_{L1,HLT} = 1$ for a specific trigger, it is said to be unprescaled.

For instance, $1/p_{L1}$ defines the number of events passing by L1 and that can be then processed by the HLT. And $1/p_{HLT}$ defines the number of events passing an L1 selection required by an HLT chain and that can be then processed at the HLT.

The building blocks on which the trigger menu lies on are :

- primary triggers, which are unprescaled and are run for physics analyses.
- support triggers for efficiency and background studies
- alternative triggers, which are experimental (new) reconstruction algorithms
- backup triggers that use tighter selections
- calibration triggers to calibrate the detector

Selections that are paramount in this study are the ones involving jets, which are reconstructed with the anti-k_t algorithm[18] and with either $R = 0.4$ or $R = 1.0$. Two L1 items that are used mainly are `L1_4J15` and `L1_J100`, jointly with HLT selections.

More information on the trigger performance at ATLAS can be found in Refs. [19][20].

3.8 Atlas data formats

In this thesis, we used mainly two types of data to perform our analyses.

To begin with, there are the Monte Carlo (MC) samples that are very useful because they reflect perfectly into data the physics process being studied (e.g. the gluino decay in our case), such that selection criteria can be applied to increase the relevant signal when performing studies with real data. They are also used in the same fashion when an estimation of the contribution from non-desirable SM processes is needed.

These type of samples are produced in multiple steps.

The first step is the event generation. The matrix element of each process is calculated to leading order or next-to leading order using parton distribution. The same partons will therefore hadronize, creating particles that are "detected". This step relies heavily on known QCD models. The event generator packages such as PYTHIA[21] or HERWIG[22] handle this crucial part.

Then, these events are fed into a detector simulation software, which simulates the interaction of the particles with the detector material. A toolkit that is widely used for that purpose is GEANT4[23]. Every aspect such as the geometry of the system, the tracking of the particles or even the materials used in the experiment is simulated. As these particles go (virtually) through the detector and deposit their energy, the software records hits.

The next step in the production process is to digitize those hits such that the output looks like real data coming from the detector. Since ATLAS, for instance, is composed of sub-detectors, this step should be more subtle in order to mimic the data correctly. However, things like noise modeling or event pile-up need to be taken into account for the whole detector. The latter designates additional proton-proton collisions that can alter with the physics object studied. It is a major issue because subsystems tend to have sensitivity windows greater than 25 ns, which is the spacing between two bunch crossings (see beginning of this section). Simulation of

the sources of pile-up such as in-time (from the same bunch crossing) or out-of time (from adjacent bunch crossing) pile-up is a serious challenge[24].

The final step is the reconstruction that consists of the reconstruction of tracks, vertices and clusters in the subsystems and therefore the reconstruction of high-level objects such as particles or jets.

The other type of data is ATLAS reconstructed data. It is data coming directly from the detectors. These are reconstructed in the same way as MC data.

In both cases, xAOD (often abbreviated AOD) are produced. They summarize reconstructed events, accessible via the software Athena[2]. Derived AODs (DAOD) are AODs with specific selections applied.

The figure 3.8 below summarizes the production of the two types of data.

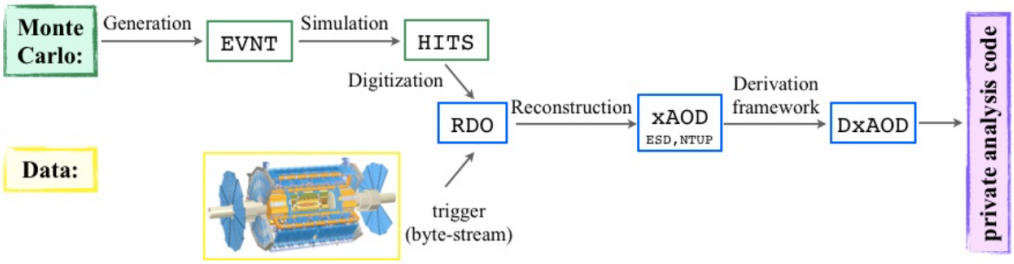

FIGURE 3.8: Different steps in the production of Monte-Carlo and reconstructed real data. Figure taken from an ATLAS twiki page.

[2]Athena is the name of the ATLAS software framework that manages almost all ATLAS production workflows: event generation, simulation, reconstruction and derivation production. Athena is also used online in the ATLAS High Level Trigger[25]

The quest of long-lived particles and delayed jets

The presentation of the LLP detector signatures is inspired from Ref. [26]. We then give a definition of the jet timing we use in this thesis. Finally, we restricted the part about published searches to only the ones using the timing of jets. An extensive review of other aspects of LLP searches can be found in the same article.

4.1 Detector signatures

The search for long-lived particles rests on correctly identifying the signatures produced by these particles as they pass through the detector. Generally, the quantities of interest are the displacement, the timing or the energy as we will see. We can also divide the detection of LLPs into two categories : the direct ones pertaining to the direct interaction of these particles with the detector material and the indirect ones corresponding to the detection of the decay products of the LLPs.

The schematic diagram below summarizes the different types of signatures that can be found.

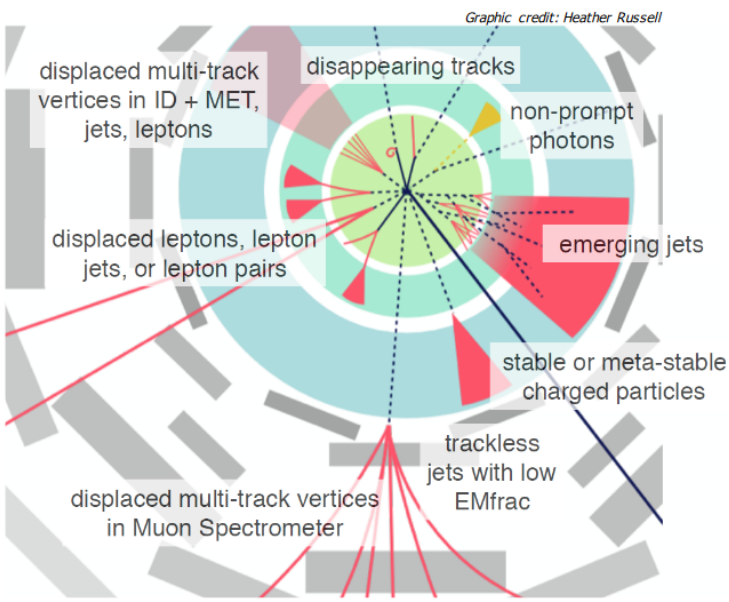

FIGURE 4.1: Detector signatures of the long-lived particles. Taken from Ref. [27, p. 9].

For example, disappearing tracks occurs when a charged LLP decays inside the identification volume such that the track seems to vanish. Generally, a neutral stable particle and an SM particle are produced. Searches at ATLAS, for long-lived charginos produced by the decay of a prompt gluino[28] were based on the reconstruction of the short track if 4 layers of the pixel detector have been hit and in association with a large missing transverse momentum and a high transverse momentum jet.

Another instance of signature is secondary long-lived particles that are produced at one point inside the detector, which is called a displaced vertex (DV). Its distance to the interaction point can be retrieved, but it involves a precise mapping of the volume. Such DV can appear in the ID or in the muon spectrometer. Studies were done at ATLAS[29], in order to reconstruct R-hadron decays happening 1 mm to 100 mm from the PV, by selecting massive displaced vertices with 5 or more outgoing tracks and a high missing transverse momentum.

It is also possible the particles decay inside the hadron calorimeter for example, resulting therefore in a low energy deposited inside the electromagnetic calorimeter. The trigger that addresses this effect is $CalRatio = E_H/E_{EM}$, which is the ratio between the energy deposited in the HCAL and the energy deposited in the ECAL. Moreover, the jets produced will tend to be narrower than the prompt ones. Searches at ATLAS[30] using these features were performed for long-lived scalars decaying into SM fermions.

Finally, when the LLP is very heavy and electrically charged, its speed will be low and thus by the Bethe-Bloch formula, the energy lost $\langle dE/dx \rangle$ will be anomalously large. Many searches at ATLAS[31][32] were focused on heavy stable charged particles, using jointly the energy lost in the silicon pixel detector and time-of-flight measurements (since $\beta < 1$). Other type of LLPs such as monopoles that, if they exist, would have an electric charge of $|z| = 68.5$, thus resulting in very high matter ionization, sparked interest at ATLAS[33].

Of course, long-lived particles are not restrained to any particular detector signature. They can manifest via aggregate signatures, meaning they can give rise to multiple and different signatures as they evolve through the detector.

In all of these scenarios, the particles created when the LLP decay, will hadronize and give rise to displaced jets and undetectable particles as explained in section 2.3.2. The things to look for are then the missing transverse energy (MET) or the transverse momentum for instance and what's this thesis focuses on, that is the timing of the jets.

Considering the fact that LLPs move slowly in the detector, the jets produced in its decay will arrive at the calorimeter later than the usual prompt jets. Here, the LLP is considered to decay close to the ECAL such that a DV can not be reconstructed.

Indeed, figure 4.2 shows, in the context of the R-hadron model (see sect.2.4), the DV reconstruction efficiency for a gluino decaying at some radial position in the detector volume. In this particular case, the tracks are reconstructed using the large-radius tracking algorithm[34]. The further away the vertex is from the PV, the lower the efficiency. Analysis using the DV reconstruction then becomes useless at large radii.

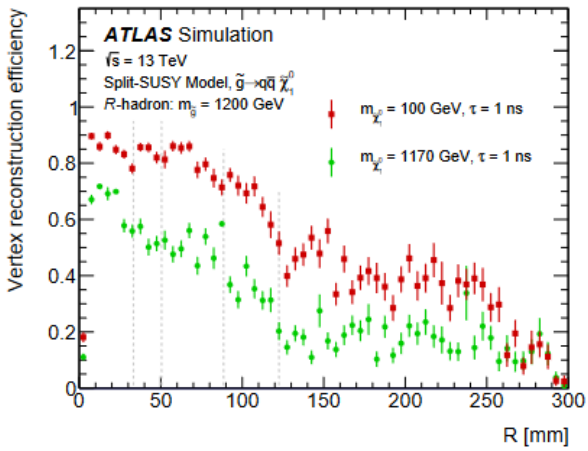

FIGURE 4.2: Vertex reconstruction efficiency for a gluino decay occurring at a radial position inside the detector. Taken from Ref. [35].

4.2 Jet timing definition

A jet is defined as an ensemble of hadrons collimated around an axis. Each particle composing the jet will arrive at some point in the detector in a given time t_P. Experimentally, the timing of the constituents is determined by the calorimeter cells. Thus, in order to avoid contribution from the background processes to the timing measurement, only cells that are comprised in the reconstructed jet are considered.

There are many ways to define the jet timing. We list only some. A more rigorous theoretical study of the jet timing can be found in Ref. [36].

In the definitions below, the index i corresponds to the cell i and N is the number of cells.

- the average time defined as the arithmetic mean over all cell timings :

$$\bar{t} = \frac{1}{N}\sum_{i}^{N} t_i$$

- the median of all the cell timings
- the energy-weighted timing, which is the arithmetic mean of all cell timings weighted by the energy of each cell involved :

$$\bar{t}_E = \frac{\sum_i^N E_i t_i}{\sum_i^N E_i}$$

With regard to the last definition, one can also define another timing by replacing $E_i \to E_i^2$. We say then that the timing is energy-squared weighted. In the Athena software, it seems that this definition is used for the jet timing as one can see in Ref. [37].

At the calorimeter level, only the cell, in the middle-layer, which has the maximum energy deposit is used in order to avoid crosstalk (interference from two signals).

4.3 Published searches using the timing of the jets

CMS[38] performed LLP searches with data of proton-proton collisions at center-of-mass energy of 13 TeV collected in 2016, 2017 and 2018.

They used the timing of energy deposits in the ECAL corresponding to delayed jets events and interpreted these results with the help of the gauge-mediated supersymmetry model (gluino decaying to a gluon and a feebly interacting gravitino). The Feynman diagram for this process is shown below:

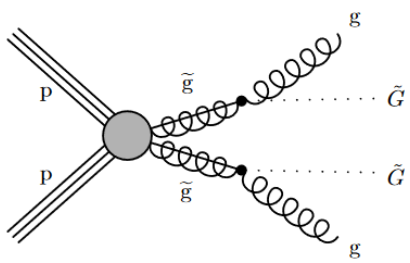

FIGURE 4.3: Feynman diagram for the GMSB signal model

The range of gluino masses extended from 1 to 3 TeV and with lifetimes between 1 and 300 ns.

The physics objects used in this study are jets i.e. energy deposits in both calorimeters and clustered by the anti-k_T algorithm with a distance parameter of 0.4. Similarly to this thesis, Particle-Flow jets[39] are not used. In the particle-flow algorithm, tracks in the ID and energy deposits in the calorimeters are linked to reconstruct particles. As explained previously, non-prompt jets can be produced outside the tracker, making this algorithm unsuitable.

Moreover, the jet timing is defined using the ECAL cells that verify $\Delta R < 0.4$ between the jet axis and the cell position and for which the energy is greater than 0.5 GeV. Deposits with $t_J > |20|$ ns are not counted in order to reject contributions from different bunch crossings. The timing of the jets t_J is the median cell time.

The signal region was defined such that the applied selections are about 90% efficient and assuring also a decrease by a factor 10 of the background event rate.

They applied baseline selections on jets such as $p_T > 30\,\text{GeV}$ and $|\eta| < 1.48$ in order to consider only jets reconstructed in the ECAL barrel. The time of the jets was required to be $t_J > 3\,\text{ns}$ so that the gluino decay close to or inside the ECAL. The energy deposited must be superior to 25 GeV and the number of cell hits must be higher than 25 in order to optimize the timing resolution

In addition, selections on the energy deposited in the HCAL and a requirement of p_T^{miss} were considered to reject further noise.

Several other selections such as the ratio between the transverse momentum of all tracks produced at the primary vertex (PV) and the transverse calorimeter energy of the jet, namely $PV_{track}^{fraction}$, were also applied to reject prompt jets.

The background estimation was done by inversion of the selection parameters. There are three main sources. The first one is the beam halo, which corresponds to muons produced by the collision between the beam protons and collimator and which pass through the ECAL, resulting in an early or late signal. Usually beam halos are characterized by a low hadronic energy fraction.

The second one pertained to out-of-time jets coming from the collision of protons residing in lowly filled adjacent bunches. Such objects have generally a large $PV_{track}^{fraction}$.

Finally, cosmic ray muons can also contribute to the total energy in the ECAL. ϕ selections on the muon system were considered.

The table 4.1 shows the contribution from the various backgrounds. The total background yield is $1.1^{+2.5}_{-1.1}$ events.

Background source	Events predicted
Beam halo muons	$0.02^{+0.06}_{-0.02}$ (stat)$^{+0.05}_{-0.01}$ (syst)
Core and satellite bunch collisions	$0.11^{+0.09}_{-0.05}$ (stat)$^{+0.02}_{-0.02}$ (syst)
Cosmic ray muons	$1.0^{+1.8}_{-1.0}$ (stat)$^{+1.8}_{-1.0}$ (syst)

TABLE 4.1: Estimation of the contribution from the different background sources in the CMS paper.

The figure 4.4 below shows two events recorded by CMS and the contributions from signals and backgrounds. The black line represents the jet timing cut at 3 ns. Zero events are observed passed that line.

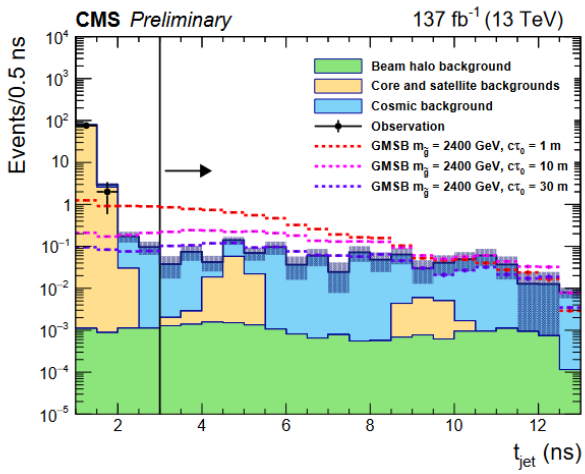

FIGURE 4.4: Jet timing distribution of both signal and background processes and events observed by CMS.

Monte-Carlo studies

This chapter's goal is to find out which Level-1 item used in conjunction with HLT selections should be implemented later on in the trigger menu. Moreover, it is equally important to quantify the cut in the jet timing, which enhances the signal region and at the same time allows for an optimal background rejection.

5.1 Signal and background samples

The signal samples used were Monte-Carlo samples corresponding to a long-lived gluino produced in a 13 TeV proton-proton collision and decaying to two quarks and the lightest neutralino as predicted by the *split susy* model that was presented in section 2.4.

The gluino and the neutralino masses extend from 100 to 3000 GeV with the gluino's proper lifetime τ ranging from 10 ps to 30 ns, which translates to decay lengths ($c\tau$) between 0.003 m and 9 m. The samples were simulated via PYTHIA 8 and generated using MadGraph.

To study the background contribution, a MC sample corresponding to QCD dijets was used. It was simulated with PYTHIA 8 and generated with MadGraph.

Usually, SM processes occur promptly and a search focusing on delayed jets will inevitably reject this type of background. However, as can be seen in the figures 5.1a and 5.1b, there is a non-negligible presence of dijets at large timing and low p_T and thus will constitute an important source of background.

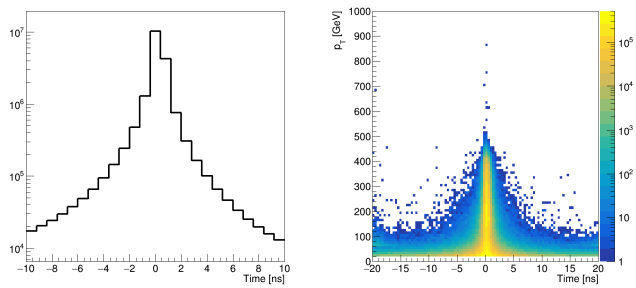

(A) (B)

FIGURE 5.1: (A)Dijet timing distribution. (B) 2d distribution of the timing and the transverse momentum.

Furthermore, the transverse momentum distribution of these dijets is divided in three p_T intervals and each event has a weight associated to it such that the distribution looks continuous. Figure 5.2 shows the total weighted p_T distribution of the leading jets.

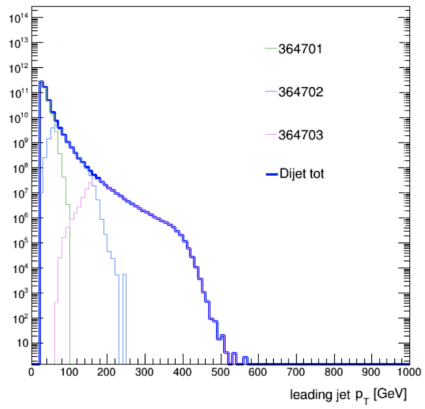

FIGURE 5.2: Leading p_T distributions of dijets.

More details about the generation of the samples can be found in the JIRA tickets [40][41].

5.2 L1 acceptance

The two L1 items that were studied are `L1_4J15` and `L1_J100`, which trigger events with at least 4 jets with $p_T > 15\,\text{GeV}$ and at least 1 jet with $p_T > 100\,\text{GeV}$, respectively.

The following acceptance was computed for each sample :

$$\mathscr{A}_{L1} = \frac{N(L1)}{N_T} \tag{5.1}$$

where $N(L1)$ is the number of L1 accepted events and N_T is the total number of events per sample.

The figures from 5.3 to 5.5 below show the L1 acceptance for different gluino lifetimes and different L1 items. Only some of them are shown, the rest can be found in appendix A.

The major observation that can be drawn is that the L1 acceptance, for both items, is the largest when the LSP mass is 100 GeV. At this mass, the acceptance increases when τ decreases or the gluino mass increases. Also, it is noticeably greater in the case of `L1_J100`.

Moreover, one can gain more insight on how $\mathscr{A}_{L1}$ depends on model parameters by looking at the acceptance at fixed lifetime or at fixed mass splitting $\Delta m = m_{\tilde{g}} - m_{\tilde{\chi}_1^0}$.

Figures 5.6 and 5.7a-5.7b display respectively how $\mathscr{A}_{L1}$ varies with $m_{\tilde{g}}$ and τ when $\Delta m = 100$ GeV and its variation with Δm and $m_{\tilde{g}}$ when $\tau = 1$ ns. Similarly, the tables 5.1-5.2 show the acceptance at different mass splittings and for different gluino masses.

In the figures 5.6a-5.6b, there are only three τ values since samples with different lifetimes do not have the targeted mass splitting. What can be gathered is that the `L1_4J15` acceptance is significantly lower at 10 ns than it is at 0.1 ns and 1 ns, for which the acceptance is approximately equal. In contrast, the `L1_J100` acceptance is almost the same for the three lifetimes. And this is also the case for different Δm.

The figures 5.7a-5.7b shows that the L1 acceptance increases as Δm increases. It goes to almost 1 for approximately $\Delta m > 1.5$ TeV. It is not surprising since we argued the acceptance increases at $m_{\tilde{\chi}_1^0} = 100$ GeV when $m_{\tilde{g}}$ increases. Indeed, the higher this mass difference, the higher the momenta of the decay products and therefore, the higher the probability that they will be triggered by a jet trigger. That's also the reason why the `L1_J100` acceptance is higher.

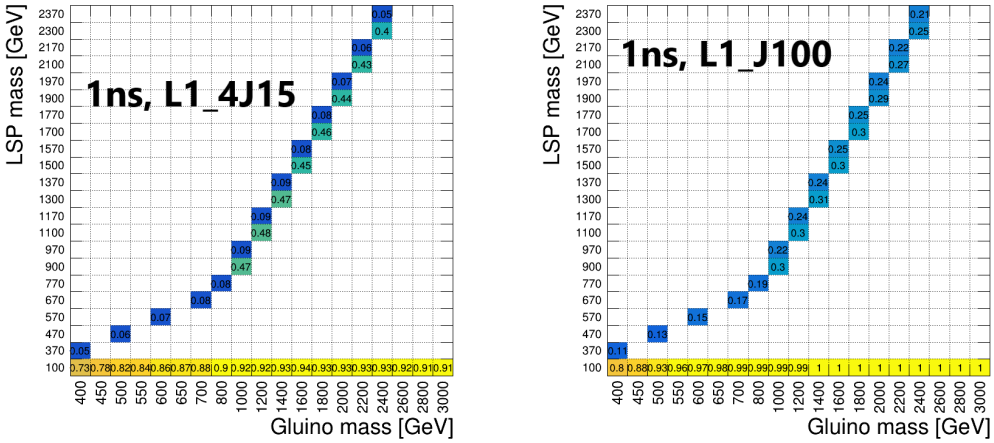

(A) `L1_4J15` (B) `L1_J100`

FIGURE 5.3: L1 acceptance for $\tau = 1$ ns.

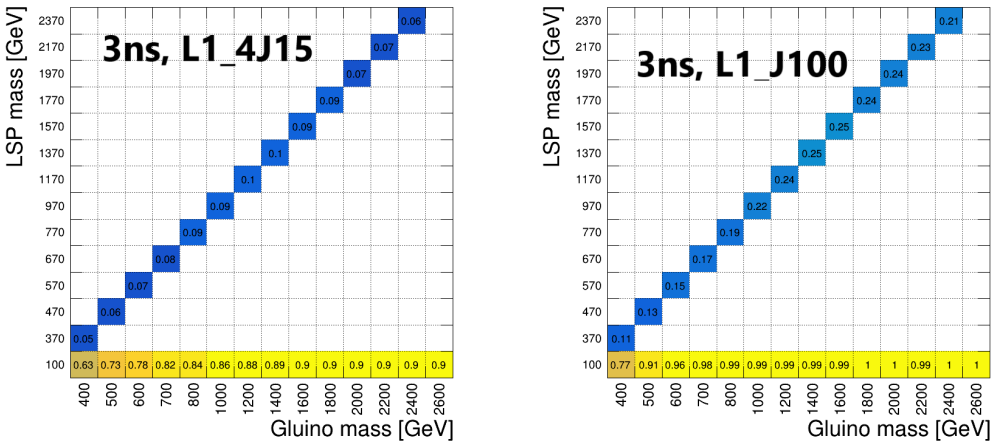

(A) `L1_4J15` (B) `L1_J100`

FIGURE 5.4: L1 acceptance for $\tau = 3$ ns.

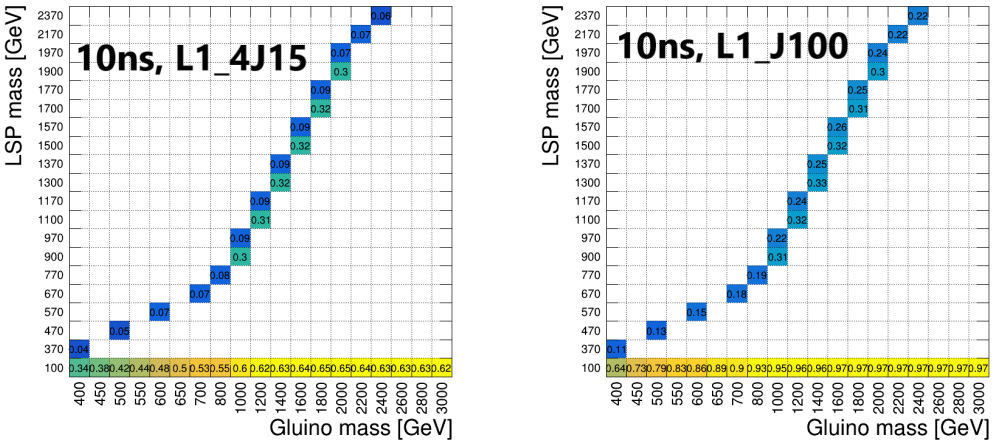

(A) L1_4J15 (B) L1_J100

FIGURE 5.5: L1 acceptance for $\tau = 10\,\text{ns}$.

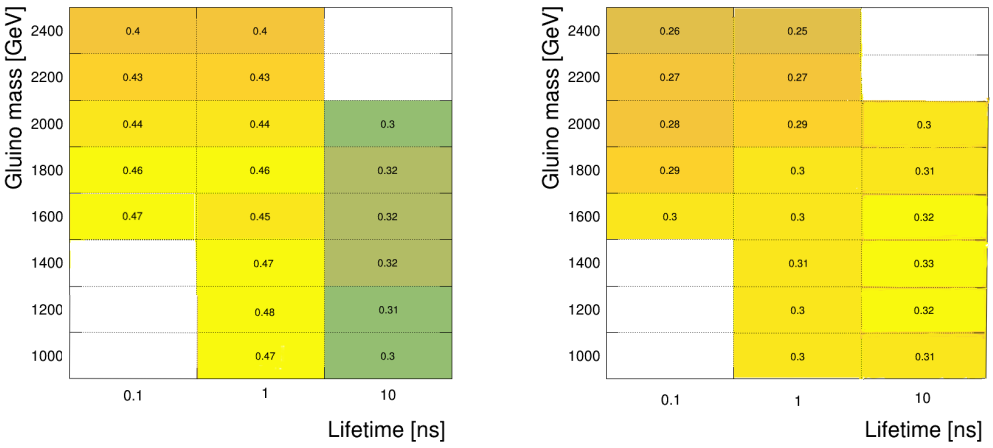

(A) L1_4J15 (B) L1_J100

FIGURE 5.6: L1 acceptance at $\Delta m = 100\,\text{GeV}$.

	0.1 ns	1 ns	10 ns
(1600,500), (600,500), (600,500)	0.88	0.86	0.48
$(1200, 1100)_2$		0.92	0.62
$(2000, 1900)_3$	0.93	0.93	0.65
$(2600, 2500)_3$	0.92	0.92	0.63

TABLE 5.1: L1_4J15 acceptances for different mass splittings. For each row, the left most cell specify $m_{\tilde{g}}$ and Δm for each τ.

	0.1 ns	1 ns	10 ns
(1600,500), (600,500), (600,500)	0.99	0.97	0.86
$(1200,1100)_2$		0.99	0.96
$(2000,1900)_3$	1	1	0.97
$(2600,2500)_3$	1	1	0.97

TABLE 5.2: `L1_J100` acceptances for different mass splittings.

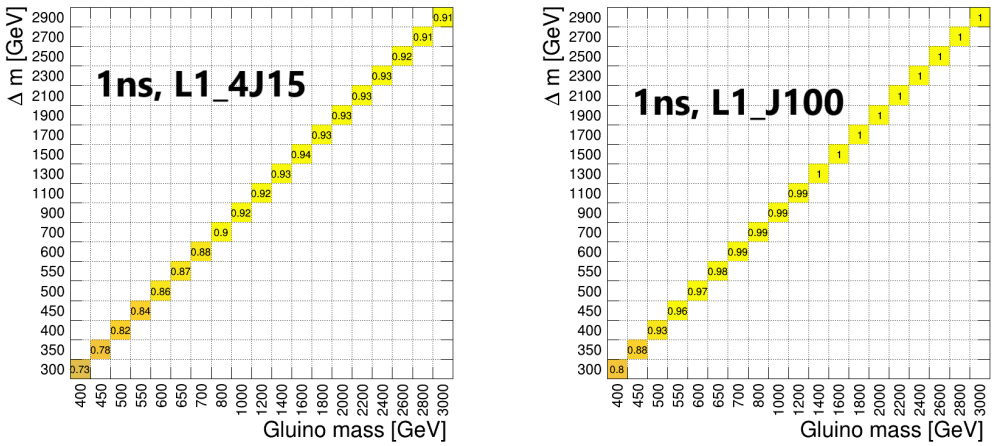

(A) `L1_4J15` (B) `L1_J100`

FIGURE 5.7: L1 acceptance as a function of Δm at $\tau = 1\,\text{ns}$.

5.3 Acceptance of jet selections

We want here to compare a multi (single)-jet trigger to a missing transverse momentum trigger that are often used in LLP searches.

Tables 5.3 and 5.5 show the acceptance of some E_T^{miss} and jet selections for the two mass splittings $\Delta m = 100$ GeV and $\Delta m = 1900$ GeV. For instance, j200 means at least one jet with $p_T > 200$ GeV and MET200 corresponds to $E_T^{miss} > 200$ GeV. The latter and MET250 correspond to selections for which the missing-E_T triggers are fully efficient.

The acceptance is defined as:

$$\mathscr{A}_{sel} = \frac{N_{sel}}{N_T} \tag{5.2}$$

where N_{sel} is the number of events per sample that verify the selection condition.

Tables 5.4 and 5.6 display the fraction of events that verify a jet selection OR an E_T^{miss} cut. The two right-most columns specify the increase of acceptance we get with respect to a multi-jet selection when considering an OR condition between the same selection and a MET one. We do not show the columns for the single-jet selection because the acceptance do not increase significantly.

For both Δm, the selections' acceptance is higher at low lifetime and $4j50$ exhibits the lowest one. For the low mass splitting, the selection with the greatest acceptance

overall is MET200, although it is not exactly the case for the high mass splitting. However, we observe clearly that the acceptance is higher at large Δm. When an OR condition is applied between a multi-jet and an MET trigger, we see the acceptance increases noticeably.

$m_{\tilde{g}}$ [GeV]	$\tau[ns]$	4j50	j200	MET200	MET250
1600	0.1	0.18	0.19	0.25	0.17
2400	0.1	0.13	0.17	0.22	0.16
1000	1	0.17	0.17	0.22	0.14
2000	1	0.15	0.19	0.24	0.16
1000	10	0.11	0.18	0.22	0.15
2000	10	0.11	0.19	0.24	0.16

TABLE 5.3: Acceptance for different E_T^{miss} and jet selections at $\Delta m =$ 100 GeV.

$m_{\tilde{g}}$ [GeV]	$\tau[ns]$	$4j50\|\|MET200$	$4j50\|\|MET250$	$\mathscr{R}[4j50\|\|MET200]$	$\mathscr{R}[4j50\|\|MET250]$
1600	0.1	0.33	0.28	+83%	+56%
2400	0.1	0.28	0.23	+115%	+77%
1000	1	0.3	0.25	+76%	+47%
2000	1	0.3	0.25	+100%	+77%
1000	10	0.26	0.21	+136%	+91%
2000	10	0.28	0.22	+154%	+100%

TABLE 5.4: The columns $\alpha||\beta$ give the acceptance for the events that satisfy the selection α OR the selection β. The columns $\mathscr{R}[\alpha||\beta]$ give the relative increase of acceptance of the OR selection with respect to $4j50$. The columns for $j200$ are not shown since there is no major increase. Here for $\Delta m = 100$ GeV.

$m_{\tilde{g}}$ [GeV]	$\tau[ns]$	4j50	j200	MET200	MET250
2000	0.1	0.91	1	0.95	0.93
2000	1	0.91	1	0.94	0.92
2000	10	0.66	0.97	0.92	0.88

TABLE 5.5: Acceptance for different E_T^{miss} and jet selections at $\Delta m =$ 1900 GeV.

$m_{\tilde{g}}$ [GeV]	$\tau[ns]$	$4j50\|\|MET200$	$4j50\|\|MET250$	$\mathscr{R}[4j50\|\|MET200]$	$\mathscr{R}[4j50\|\|MET250]$
2000	0.1	0.99	0.99	+9%	+9%
2000	1	0.99	0.99	+9%	+9%
2000	10	0.96	0.95	+45%	+44%

TABLE 5.6: Condition OR and relative increase for selections on models with $\Delta m = 1900$ GeV.

5.4 Timing cut

5.4.1 Signal

One can look at how the acceptance evolves for L1 accepted events when a timing cut is evaluated. The idea here is to find which cut in the signal region gives the best acceptance with respect to parameters such as the mass splitting or the gluino's proper lifetime.

Figures 5.8b and 5.8a show the maximum timing per event for low and high Δm respectively and considering all the events in the sample. On each plot that follows in this section, the gluino mass is indicated by m and the neutralino mass by m_{LSP}.

The strategy is to look at which model parameters tend to give jets with a large timing. We observe that at equal $m_{\tilde{g}}$ and τ, the maximum timing distributions for low Δm samples tend to be narrower and don't spread as much as the high Δm samples.

Also, we see that the high τ models have a bigger tail. Indeed, as the gluino proper lifetime increases, the distance travelled ($d = \gamma\beta c\tau$) by the gluino will be large, and we should expect that the number of jets with a large timing increases too. For the same reason, the lighter gluino's jets will contribute more at large timings since the gluino's boost is higher.

A peculiarity that we failed to understand is the small collapse of the curves at $t \approx 14\,\text{ns}$.

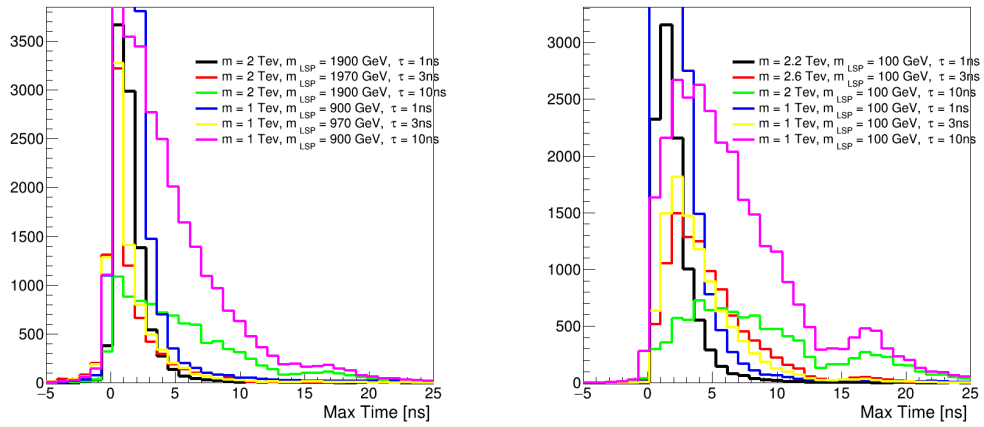

(A) Low Δm (B) High Δm

FIGURE 5.8: Maximum timing distribution for samples with (a)low and (b)high mass splittings. No L1 trigger is applied here.

The acceptance per sample is therefore defined as :

$$\mathscr{A}_{L1}^{tc} = \frac{N(t_{max} > x|L1)}{N_T} \tag{5.3}$$

with $N(t_{max} > x|L1)$ being the number of L1 accepted events that survive the timing cut. Note that when the timing cut is evaluated, the maximum timing per event is considered, meaning that if for one event $t_{max} > t_{cut}$, the event is accepted, otherwise it is discarded. We want here to look at the most delayed jets, hence the cut in the maximum timing.

Figures 5.9a-5.9b and 5.10a-5.10b show $\mathscr{A}_{L1}^{tc}$ as a function of the timing cut for two categories of models, namely the ones with a gluino less or bigger than 1.5 TeV. As we will see in the next section, the region we would to target corresponds to a timing cut between 2 and 5 ns. The curves in each figure are given for two different lifetimes (1 and 10 ns) and different mass splittings.

In the four cases, the samples with the lowest Δm have the lowest acceptance. We can compare for instance in the two plots of figure 5.9, the curves for $\tau = 10$ ns. From the previous discussion, we would expect that the model with a gluino mass of 0.55 TeV to have more jets with larger timings than the model with $m = 1.2$ TeV. But because we require also that the events are triggered by one of the L1 items, then it makes sense that the one with a higher gluino mass have a larger acceptance. On the contrary, as Δm gets bigger, the acceptance increases and is a relative maximum when it is greater than 2 TeV. We can infer that samples with lower gluino masses will tend to have a lower p_T at large timings, as the 2d plots of the maximum time and p_T in figure 5.11 show. This is reminiscent of figure 5.1b, which showed a similar spread at low momentum.

Furthermore, when `L1_4J15` is considered and all other things being equal, the samples with a greater lifetime tends to have a lower acceptance, as opposed to `L1_J100` where the difference is not obvious.

Overall, it seems $\mathscr{A}_{L1}^{tc}$ is greater when `L1_J100` is considered and when Δm and τ are respectively high and low. The influence of the gluino mass is however not very clear. Thus, one can expect, a high acceptance at a low timing cut for `L1_J100` accepted events.

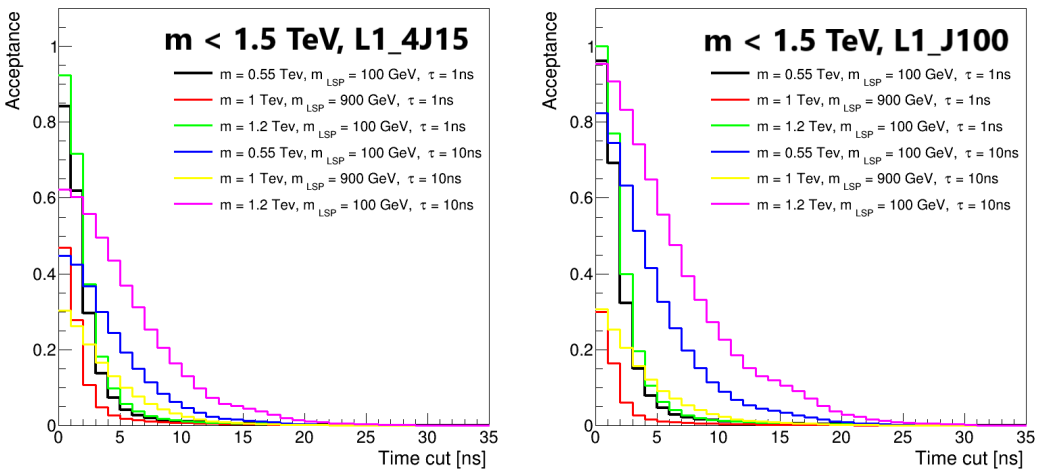

(A) `L1_4J15` (B) `L1_J100`

FIGURE 5.9: Acceptance on top of the two L1 items for different timing cuts considering $m_{\tilde{g}} < 1.5$ TeV.

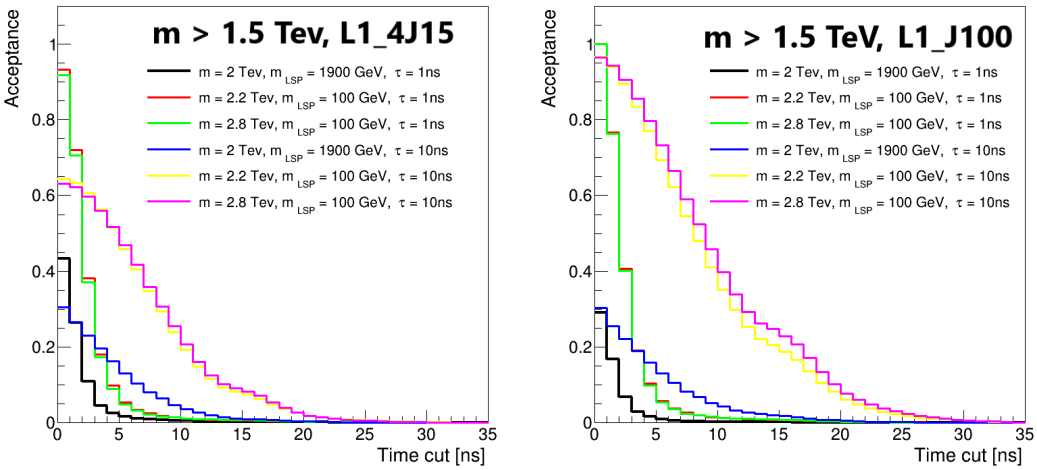

(A) L1_4J15 (B) L1_J100

FIGURE 5.10: Acceptance on top of the two L1 items for different timing cuts considering $m_{\tilde{g}} > 1.5$ TeV.

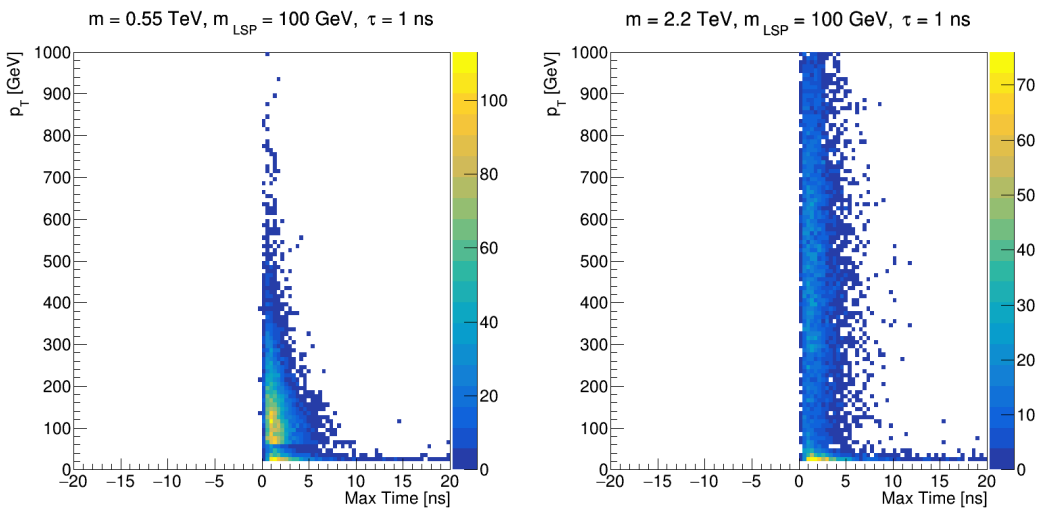

(A) (B)

FIGURE 5.11: 2d distribution of the maximum time and the transverse momentum for a (A) 0.55 TeV gluino and (B) a 2.2 TeV gluino, decaying both to a 100 GeV neutralino in 1 ns.

5.4.2 Background

Figures 5.12a and 5.12b shows the level-1 physics trigger rates for different items of which `L1_4J15` and `L1_J100`. Both have a rate of 4 kHz approximately.

The goal of this study to achieve an L1 rate of 5-10 Hz, which is of the same order of magnitude as existing triggers[42]. The background rejection factor must be between 10^2 and 10^3.

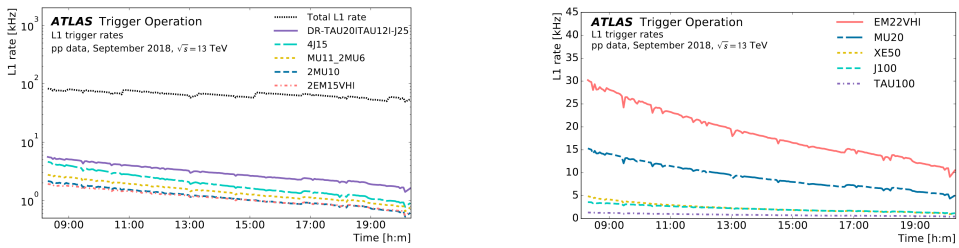

(A) `L1_4J15` (B) `L1_J100`

FIGURE 5.12: Trigger rates of some Level-1 items as a function of time in a fill taken in September 2018 with a peak luminosity of $L = 2.0 \times 10^{34} \mathrm{cm}^{-2}\,\mathrm{s}^{-1}$. From Ref. [43].

This rejection factor was plotted as a function of the timing cut and for different selections on top of either `L1_4J15` or `L1_J100`, as shown in figures 5.13a and 5.13b. The gray area in each figure is the rejection that should be achieved. For the purpose of getting the best rejection possible, we aim mostly at the top of the band.

Two types of selections were studied :

- the events for which the four (or one) leading jets have transverse momenta greater than some threshold. Then, for these events only, the maximum timing of the four (one) leading jets must be greater than the timing cut. They are designated by the nomenclature 4j50 for instance.
- the events for which there are any four jets with transverse momenta greater than some threshold and for these events only, the maximum timing of all the jets with $p_T > 50, 80$ GeV must be greater than the timing cut. They are designated by the nomenclature (4j50, all > 80) for example.

The rejection factor was defined as:

$$R = \frac{N_{L1}}{N_{sel}} \tag{5.4}$$

where N_{L1} is the number of L1 accepted events and N_{sel} is the number of events (from the subset corresponding to one selection) that survived the timing cut.

For both cases, j200 is the selection that exhibits the highest rejection and (j200, all>50) the lowest one. Moreover, all but j200 show good rejection at a timing cut of 2 ns when they are considered on top of `L1_J100`. We should then consider a cut in the timing between 2 and 3 ns.

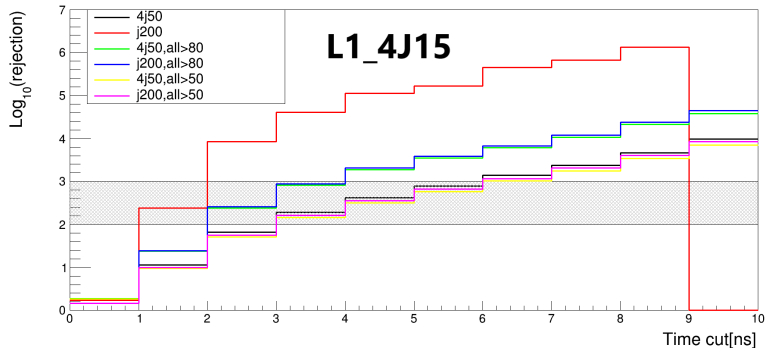

(A)

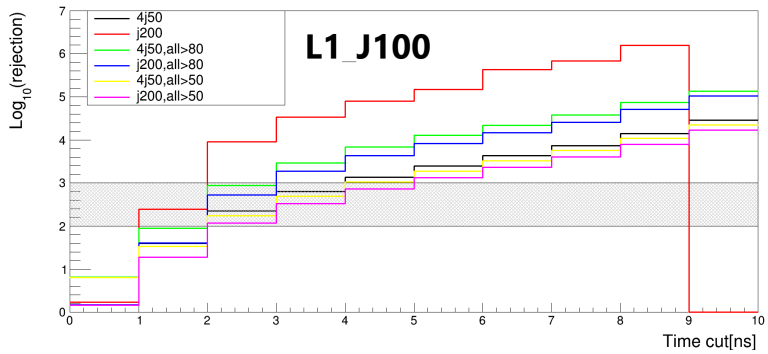

(B)

FIGURE 5.13: Rejection factor as a function of the timing cut for different jet selections on top of (A)`L1_4J15` and (B)`L1_J100`. The gray area on the plots is the desired rejection.

Study of the online jet timing

6.1 Adding the timing variable to the Athena software

We wanted first to understand how to retrieve the timing of the HLT jets.

We found that the timing of AntiKtEMTopo jets is calculated as a part of the jet modifier *CaloQuality*[44] in *JetRecoSequences.py* [45].

Next, we added the timing variable to the trigger EDM (Event Data Model) for which the code, *TriggerEDMRun3.py* can be found at Ref. [46]. More specifically, we added the element *"Timing"* to the lists **JetVarsToKeep** and **JetCopyVarsToKeep**. The image below is a screenshot of the few lines from the code we modified.

```
JetVarsToKeep = ['ActiveArea', 'ActiveArea4vec_eta', 'ActiveArea4vec_m', 'ActiveArea4vec_phi', 'ActiveArea4vec_pt', 'AlgorithmType',
                 'DetectorEta', 'DetectorPhi', 'EMFrac', 'EnergyPerSampling', 'GhostTrack', 'HECFrac', 'InputType',
                 'JetConstitScaleMomentum_eta', 'JetConstitScaleMomentum_m', 'JetConstitScaleMomentum_phi', 'JetConstitScaleMomentum_pt',
                 'JetPileupScaleMomentum_eta', 'JetPileupScaleMomentum_m', 'JetPileupScaleMomentum_phi', 'JetPileupScaleMomentum_pt',
                 'JetEtaJESScaleMomentum_eta', 'JetEtaJESScaleMomentum_m', 'JetEtaJESScaleMomentum_phi', 'JetEtaJESScaleMomentum_pt',
                 'JetGSCScaleMomentum_eta', 'JetGSCScaleMomentum_m', 'JetGSCScaleMomentum_phi', 'JetGSCScaleMomentum_pt',
                 'Jvt', 'JVFCorr', 'JvtRpt', 'NumTrkPt500', 'NumTrkPt1000', 'SizeParameter', 'SumPtTrkPt500', 'SumPtTrkPt1000', 'TrackWidthPt1000', 'SumPtChargedPFOPt500','Timing'
]
JetVarsToKeep += [f'fastDips_p{x}' for x in 'cub']
JetVars = '.'.join(JetVarsToKeep)

JetCopyVarsToKeep = ['pt', 'eta', 'phi', 'm',
                     'JetPileupScaleMomentum_eta', 'JetPileupScaleMomentum_m', 'JetPileupScaleMomentum_phi', 'JetPileupScaleMomentum_pt',
                     'JetEtaJESScaleMomentum_eta', 'JetEtaJESScaleMomentum_m', 'JetEtaJESScaleMomentum_phi', 'JetEtaJESScaleMomentum_pt',
                     'JetGSCScaleMomentum_eta', 'JetGSCScaleMomentum_m', 'JetGSCScaleMomentum_phi', 'JetGSCScaleMomentum_pt',
                     'Jvt', 'JvtRpt','Timing'
                    ]
JetCopyVars = '.'.join(JetCopyVarsToKeep)
```

FIGURE 6.1: Screenshot of a piece of code from TriggerEDM-Run3.py. The timing variable was added to both lists **JetVarsToKeep** and **JetCopyVarsToKeep**.

Finally, we also added *"Timing"* to the **floatAccessors** in the header file *TriggerEDMAuxAccessors.h* [47].

A summary of the merge request can be found at Ref. [48].

6.2 Data and MC samples

20 xAODs ($\approx 120k$ events) with the offline and online jet timings and corresponding to data taken in 2018 at 13 TeV were reconstructed.

The jet containers used in this study for the online and offline jets are respectively `HLT_AntiKt4EMTopoJets_subjesIS` and `AntiKt4EMTopoJets`.

For comparison, we used 100 Monte-Carlo samples ($\approx 50k$ events) generated through a $t\bar{t}$ process with pile-up. We studied this type of process and not dijets as in the previous chapter because these samples are easier to study, and we had a lot at our disposal. Also, $t\bar{t}$ processes give rise to multi-jets and missing transverse energy, which are some things that we already look for.

6.3 Online/offline jet timing correlation

In a perfect world, the online and offline variables are perfectly equal. The variables are for example the p_T of the jets or in our case the timing.

In real life, the situation is more complicated and some discrepancy between the two usually exists. An illustrative example is shown in figure 6.2 below. The goal is then to transform the left figure into the right one, by using the appropriate selections.

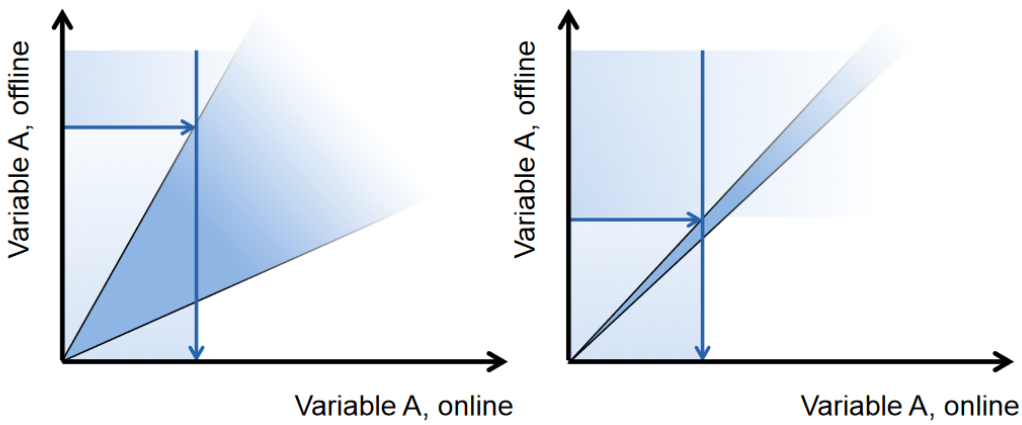

FIGURE 6.2: Illustrative example of two plots showing (LEFT) a bad correlation and (RIGHT) a fairly good correlation between an offline and online variable. From Ref. [49, p. 75].

The jets are in addition R-matched, meaning the *distance* ΔR between the two type of jets must be smaller than some threshold in order to ensure that the jets go approximately through the same region in the detector. In this thesis, the matching condition is $\Delta R < 0.4$.

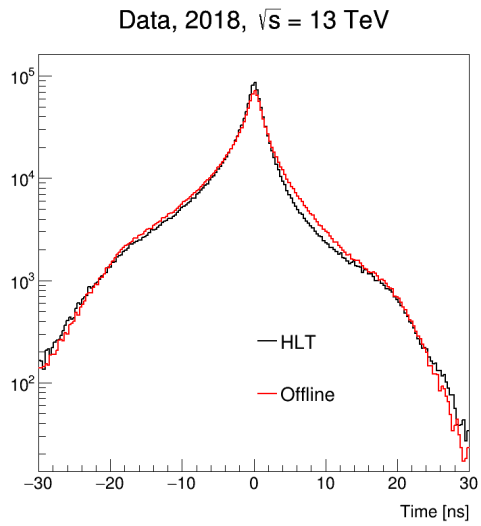

FIGURE 6.3: Timing distribution of matched online and offline jets.

Figure 6.3 shows the timing distribution of online and offline jets that are matched.

In addition, it is required that the selection applied on both online and offline jets should be fully efficient. The efficiency ε in our case is defined as:

$$\varepsilon = \frac{N(X_{offline}|X_{online} > \alpha)}{N(X_{offline})} \tag{6.1}$$

With $N(X_{offline}|X_{online})$ being the number of offline jets R-matched with online jets satisfying some condition $X_{online} > \alpha$. Here, X designates a variable.

$N(X_{offline})$ is the total number of offline jets that are R-matched.

Thus, for each value of the variable X, the efficiency takes a specific value. The variable that is considered for the x-axis is the offline one. An ideal curve for ε looks like a step-function, such that the vertical part rises at the value at which the cut in the online variable is applied. The horizontal part after that cut, where $\varepsilon = 1$, is called the *plateau*.

This is the region that is targeted. Performing then a selection on the offline variable to be in the *plateau*, should bring the offline and online variables closer to each other.

Accordingly, figure 6.4a shows the efficiency as a function of the offline jet p_T and with the online jet $p_T > 50\,\text{GeV}$. The curve looks almost like a step-function, and therefore applying also a cut at 60 GeV to the offline jet p_T guarantees a 100% efficiency. Low cuts in the transverse momentum are preferable since they don't reduce drastically the number of events.

Figure 6.4b shows the efficiency as a function of the offline jet timing for three different selections applied to the online jet timing (1,2 and 3 ns), without p_T cuts. Compared to p_T turn-on curve, there are inefficiencies. The plateau is not exactly flat and at the cut, the curve is not as steep.

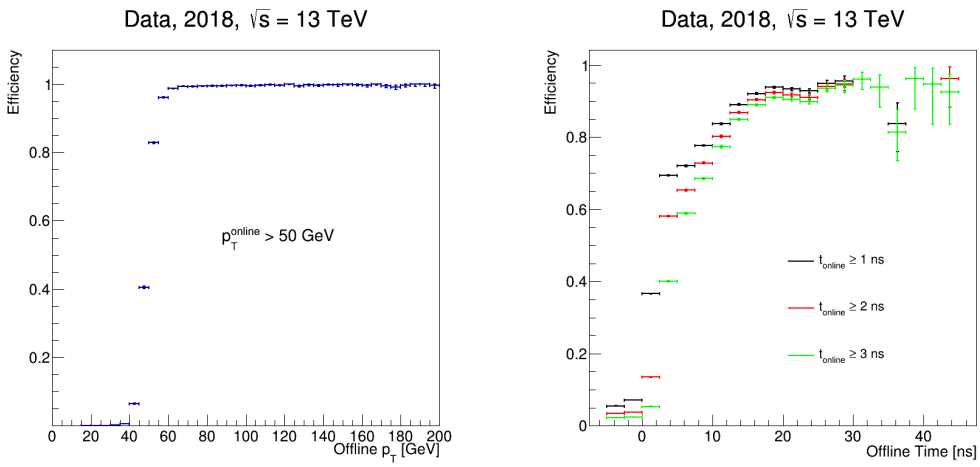

(A) (B)

FIGURE 6.4: (A)Turn-on curve of the offline jet p_T considering for the online jets $p_T > 50\,\text{GeV}$. (B) Turn-on curve of the offline jet timing considering the online timing greater than 1,2 and 3 ns and no p_T cuts.

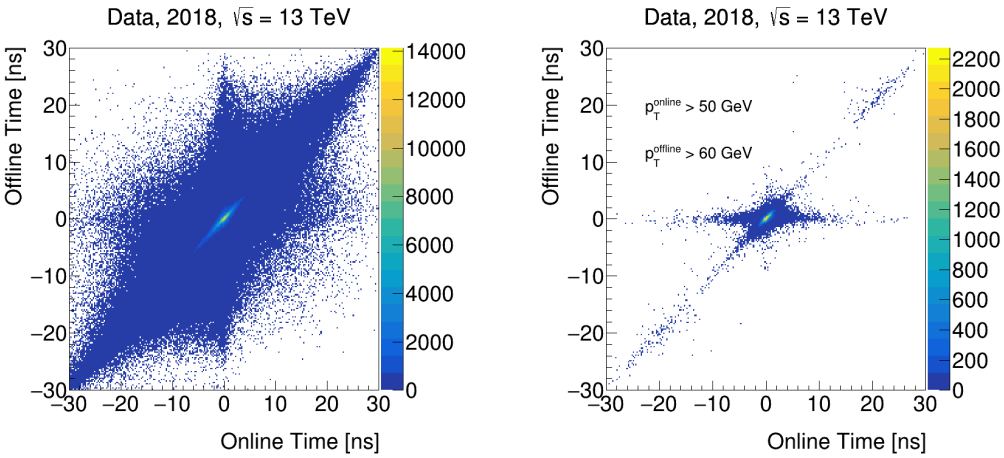

(A) (B)

FIGURE 6.5: 2d distribution of the online and offline jet timing (A) without any selection and (B) with $p_T^{online} > 50\,\text{GeV}$ and $p_T^{offline} > 60\,\text{GeV}$.

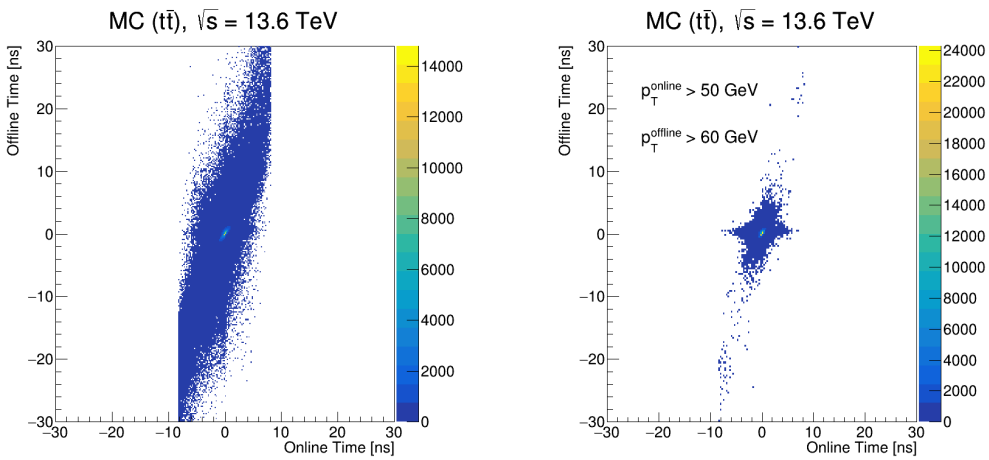

(A) (B)

FIGURE 6.6: MC correlation plots of the online and offline jet timing (A) without any selection and (B) with $p_T^{online} > 50\,\text{GeV}$ and $p_T^{offline} > 60\,\text{GeV}$. The event cut at 9 ns is something that we do not understand yet.

Figures 6.5a and 6.5b display respectively the correlation plots of the online and offline jet timings without any cut and with the selections $p_T^{online} > 50\,\text{GeV}$ and $p_T^{offline} > 60\,\text{GeV}$. We would expect the data in the right plot to be focused around a diagonal of slope 1. However, some events at $t_{offline} \approx 0\,\text{ns}$ subsist (the horizontal line). We see also on the left plot a vertical line at $t_{online} \approx 0\,\text{ns}$ that seems to vanish more or less after the p_T cut.

Figures 6.6a and 6.6b shows the same plots but for Monte-Carlo generated events. These samples were produced in a recent campaign, and they are intended for Run-III analysis.

The distributions are radically different from the previous one. Indeed, in MC, there is a cut at approximately 9 ns and the online and offline timing do not seem to follow the same trend.

Therefore, it seems that these particular MC are not the perfect benchmark to compare data to.

Figures 6.7a and 6.7b show the fraction of online and offline events that have a timing below some threshold, with and without a p_T cut (the same as in the precedent 2d plots).

Comparing the two situations, the fraction for online events is greater than the offline ones in the left plot while it is the inverse in the right plot.

At thresholds bigger or equal than 1 ns, the data with a cut in the transverse momentum manifests a higher fraction, revealing that the cut rejects most of the events with a high timing. The fractions at 0 ns are not at 50% since the distributions are not Gaussian as expected from figure 6.3.

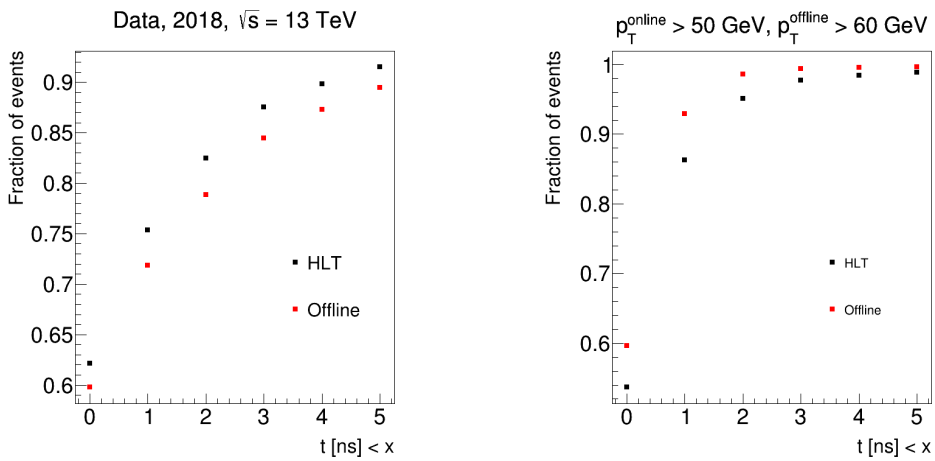

(A) (B)

FIGURE 6.7: Fraction of events as a function of different online and offline timing thresholds. (A) without a p_T cut and (B) with $p_T^{online} > 50\,\text{GeV}$ and $p_T^{offline} > 60\,\text{GeV}$.

To investigate further these *out-of-diagonal* events (in Data), one can look at the difference in timing $\Delta t = t_{online} - t_{offline}$ as shown in figure 6.8. This was plotted for jets that verify $t_{online} > 2\,\text{ns}$ i.e. for the jets that are mostly on the right side of the 2d plots.

In the best case scenario, it should look like a peak centered at $\Delta t = 0\,\text{ns}$ but here, the distribution is skewed towards the higher timing differences, thus reflecting the presence of the horizontal line.

Therefore, we need to understand the properties of these events and find if a particular region in the detector contributes.

Figure 6.9 shows the p_T, η and ϕ distributions of the leading online and offline jets while figure 6.10 shows the same properties but considering all jets.

We observe that the events, both online and offline and with $|\Delta t| > 5$ ns, tend to be concentrated in the region $|\eta| < 2$ (the two peaks in the η plot) and at low p_T for the leading jets. The p_T cuts already provide a partial rejection of these events.

Increasing the p_T selection would decrease the statistics too much. The next step is therefore to perform η cuts. Accordingly, figure 6.11 shows the 2d plot with $p_T^{online} > 50\,\text{GeV}$, $p_T^{offline} > 60\,\text{GeV}$ and $|\eta| > 1.5$ to both online and offline jets. The latter is not too harsh in order to not depopulate the correlation plot.

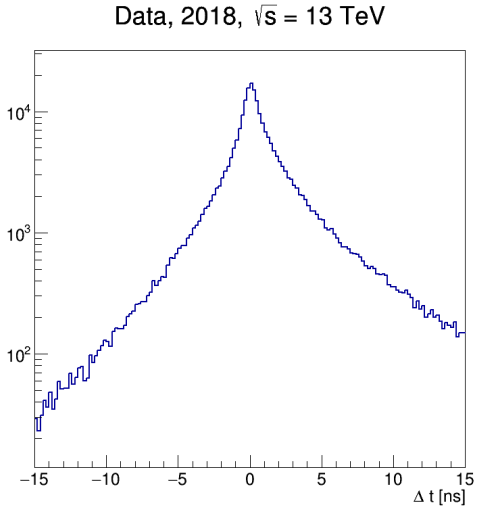

FIGURE 6.8: $\Delta t = t_{online} - t_{offline}$ distribution for $t_{online} > 2\,\text{ns}$

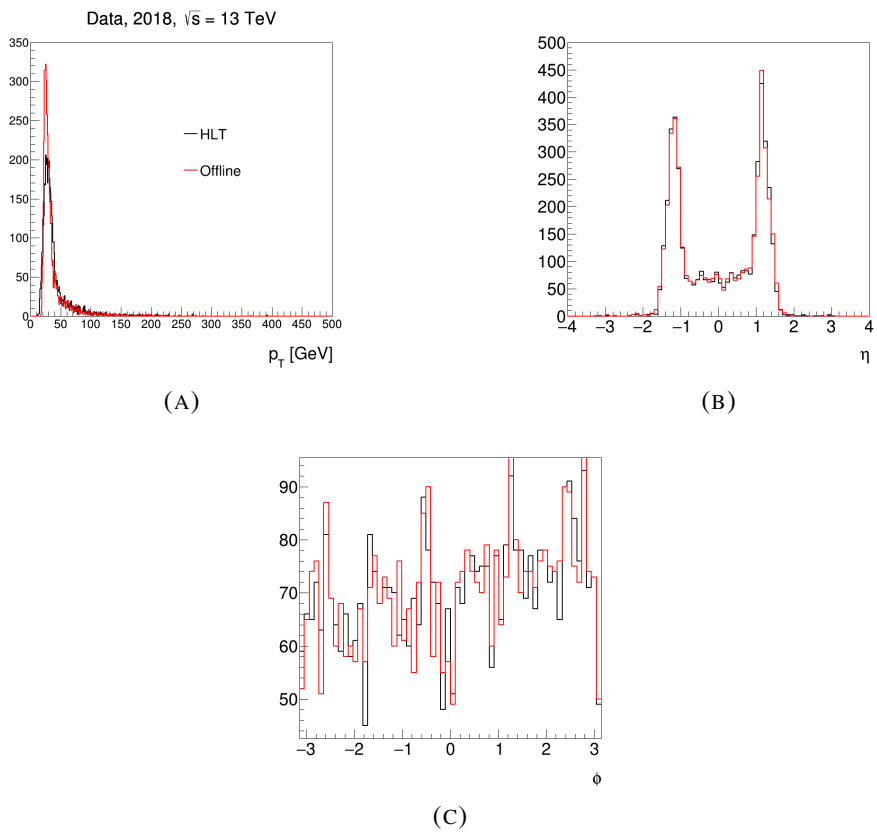

FIGURE 6.9: (A) p_T, (B) η and (C) ϕ distributions for online (black) and offline (red) **leading** jets satisfying $|\Delta t| > 5\,\text{ns}$. No p_T cuts applied.

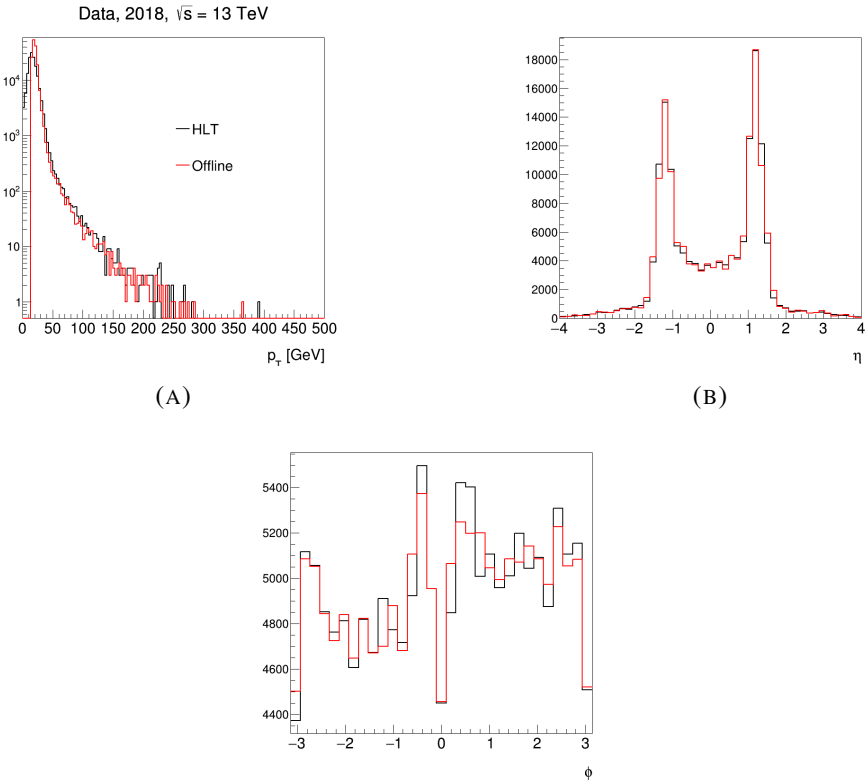

(A) (B)

(C)

FIGURE 6.10: (A) p_T, (B) η and (C) ϕ distributions for online (black) and offline (red) jets satisfying $|\Delta t| > 5\,\text{ns}$. No p_T cuts applied.

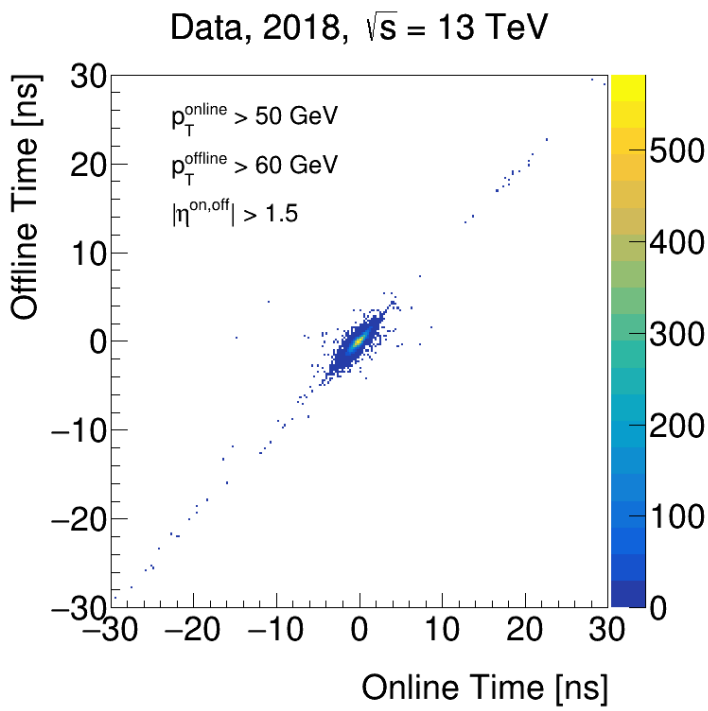

FIGURE 6.11: Online/offline correlation plot with $p_T^{online} > 50\,\text{GeV}$, $p_T^{offline} > 60\,\text{GeV}$ and $|\eta| > 1.5$ for both online and offline jets.

We observe that although the number of events is very small, there is no more a horizontal line and the vertical one completely disappeared. Thus, it seems that the cleaning selections we applied did the job more or less. However, one could object that these cuts just weeded out events and that increasing statistics would make reappear the horizontal line. This is indeed a thing that we would want to investigate in the future.

6.4 Ongoing and future work

6.4.1 Sample T studies

An important thing to note is that the MC samples that we studied previously correspond to events that are meant to have zero timing. Indeed, calorimeters are calibrated such that the timing measured for a particle traveling at the speed of light from the IP is 0 ns. Because $\beta < 1$ for LLPs, one needs to account for the jet delay in the sample. Accordingly, we requested a sample T (a sample designed for physics analyses) to be produced. It corresponds to a delayed gluino with a mass of 2.6 TeV and a lifetime of 3 ns, decaying to a neutralino with a mass of 100 GeV.

We made this choice based on the fact that a model with such parameters provide a large contribution at large timings, as can be seen in figure 6.12.

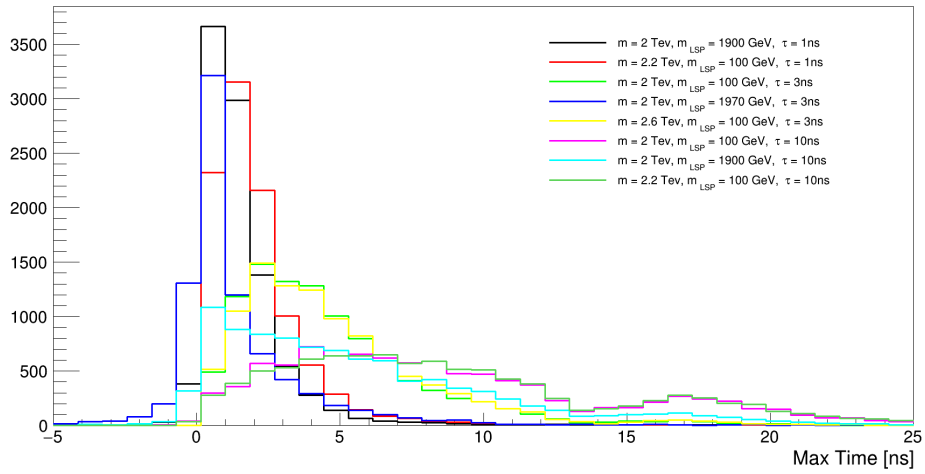

FIGURE 6.12: Maximum timing distribution of various R-hadron models

The JIRA ticket for this production campaign can be found at Ref. [50].

6.4.2 Implementation of a jet hypo algorithm

A hypothesis algorithm takes a trigger element and by accessing its characteristics, it verifies, for a region of interest, if it passes specified cuts.

Therefore, we requested the implementation of a selection on the timing of the jets in the jet hypo. The selection is simple : we require at least N jets with $p_T > A$ and with a timing $t > B$, where the units of A and B are GeV and ns, respectively.

The two trigger that we proposed are the following:

```
HLT_4j45_DELAYEDj45t2_L14J15t2
HLT_j220_DELAYEDj150t2_L1J100
```

The word DELAYED defines the scenario and t2 means $t > 2\,\text{ns}$. The first trigger requires that the 4j45 selection counts also a delayed jet, while the second trigger doesn't.

One can understand better how this triggers work by looking at some examples of events. Let's suppose, for the 4-jet trigger, that we have the event :

$$\{(45\,\text{GeV}, 0\,\text{ns}), (45\,\text{GeV}, 0\,\text{ns}), (45\,\text{GeV}, 0\,\text{ns}), (45\,\text{GeV}, 2\,\text{ns})\}$$

where each element represents a jet with some transverse momentum and timing. Then, by the trigger definition, this event pass the selection since it has at least 4 jets with $p_T > 45\,\text{GeV}$ and at least one jet with a $t > 2\,\text{ns}$. An AND condition is applied between the HLT selection and the delayed jet selection.

Accordingly, for the single jet trigger, the events

$$\{(220\,\text{GeV}, 2\,\text{ns})\}\,\text{and}\,\{(150\,\text{GeV}, 2\,\text{ns})\}$$

are respectively, passed and failed. The second event has indeed a delayed jet with $p_T > 150\,\text{GeV}$ but it does not meet the requirement that at least one jet must have $p_T > 220\,\text{GeV}$.

On the day this thesis is written, these selections are being implemented.

Conclusions

In this thesis, we used the timing of the jets measured by the ATLAS calorimeter, to study the possibility of introducing a new trigger targeting delayed jets.

We looked at Monte Carlo signal samples of a long-lived gluino decaying to two quarks and a neutralino and studied first the acceptance of the two items, `L1_4J15` and `L1_J100` as well as the acceptance of different jet selections in association with E_T^{miss} triggers. We found that `L1_J100` gives the best acceptance and that applying an OR condition between 4j50 and MET200 shows the highest increase in acceptance.

Then, we examined timing cuts in signal samples and a background sample, corresponding to QCD dijets. The cut in the maximum timing that gives a decrease by a factor 10^3 of the background is between 2 and 3 ns for different jet selections on top of `L1_J100`, allowing at the same time a good signal acceptance.

Finally, we added the timing variable to the Athena software, and we studied the correlation between online and offline jets. We found that reasonable cleaning selections are $p_T^{online} > 50\,\text{GeV}$, $p_T^{offline} > 60\,\text{GeV}$ and $|\eta^{on,off}| > 1.5$.

The next steps of this project would be to implement a trigger in the trigger menu and study its rate and its CPU cost.

The high luminosity phase of the LHC (HL-LHC) will start operating in 2026 for Run-IV. Consequently, many detector subsystems will be upgraded to account for the significant increase of pile-up. For instance, upgrade plans for ATLAS include a new high-granularity timing detector[51] that could achieve timing resolution around 30 ps and updates of the calorimeter readout electronics that could improve the timing resolution to the same orders of magnitude. The prospects for searching long-lived particles at ATLAS using timing-based triggers are therefore very interesting.

Appendices

A L1 acceptance plots

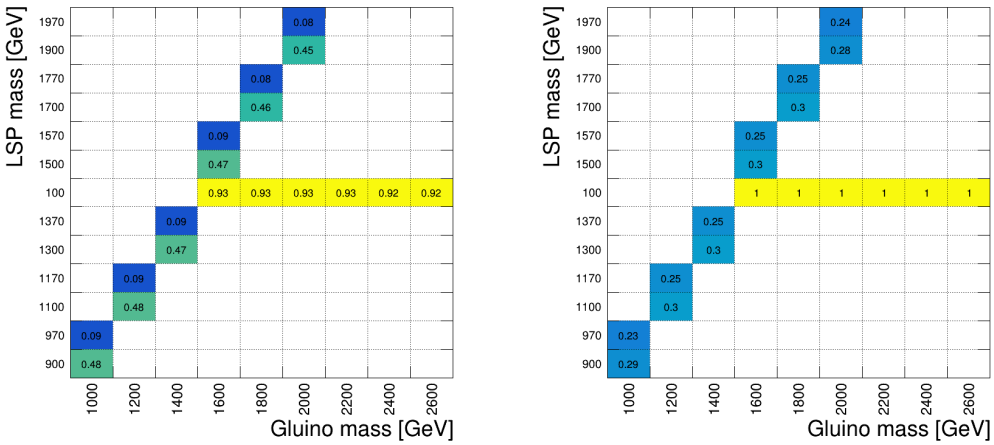

(A) L1_4J15 (B) L1_J100

FIGURE 1: L1 acceptance for $\tau = 10\,\text{ps}$.

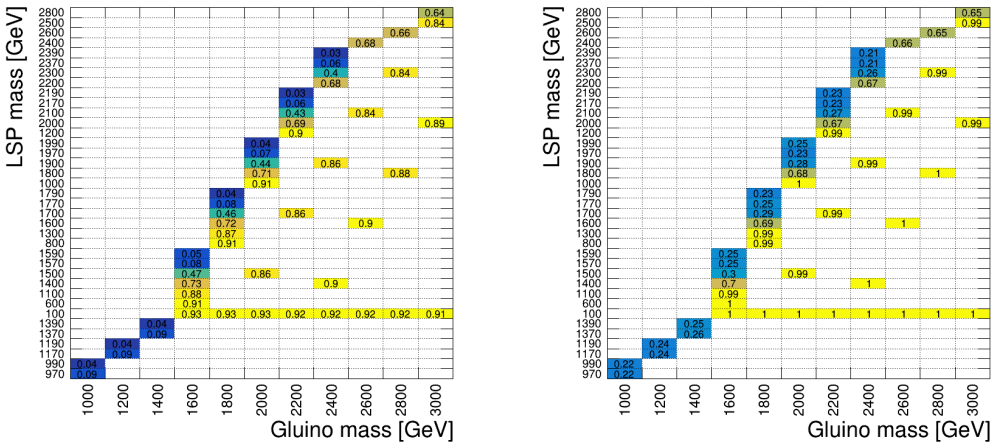

(A) L1_4J15 (B) L1_J100

FIGURE 2: L1 acceptance for $\tau = 100\,\text{ps}$.

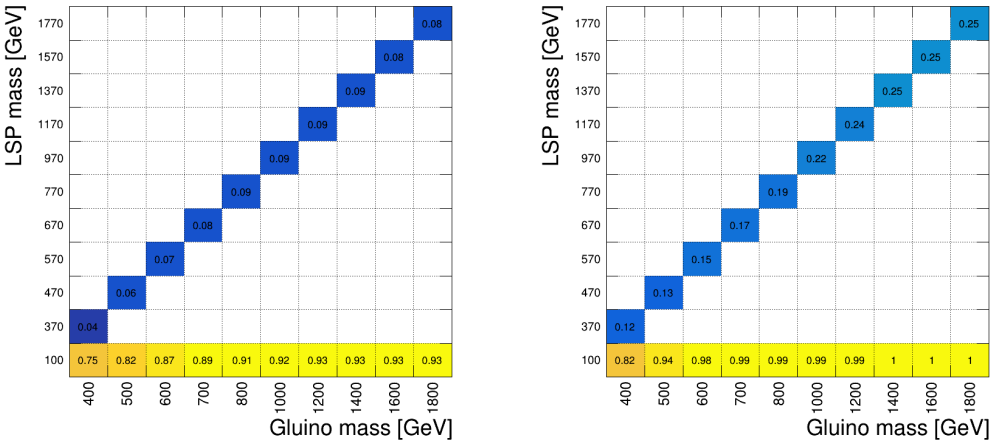

(A) L1_4J15 (B) L1_J100

FIGURE 3: L1 acceptance for $\tau = 300\,\text{ps}$.

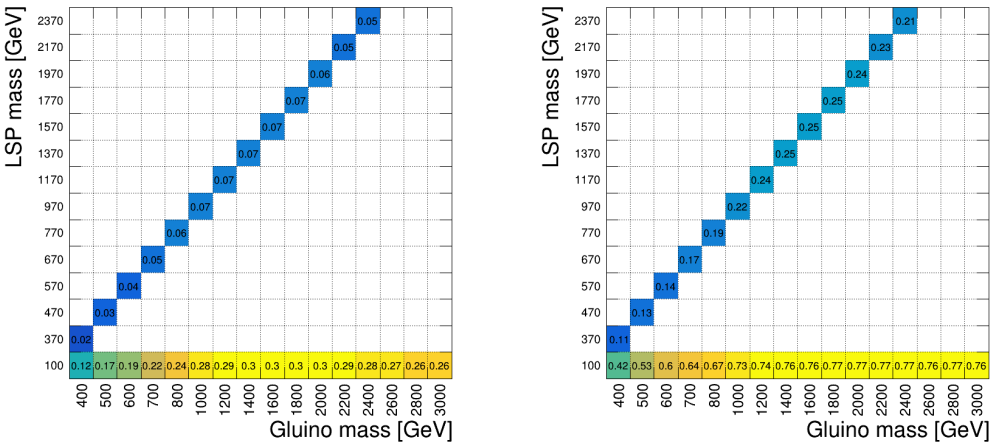

(A) L1_4J15 (B) L1_J100

FIGURE 4: L1 acceptance for $\tau = 30\,\text{ns}$.

Bibliography

[1] "Observation of a new particle in the search for the Standard Model Higgs boson with the ATLAS detector at the LHC". In: *Physics Letters B* (2014). DOI: 10.1103/physrevd.90.052004. URL: https://doi.org/10.1016\%2Fj.physletb.2012.08.020.

[2] Mark Thomson. *Modern Particle Physics*. Cambridge university press, 2013.

[3] Luc Pape and Daniel Treille. "Supersymmetry facing experiment: much ado (already) about nothing (yet)". In: *Reports on Progress in Physics* 69 (11 Nov. 2006), pp. 2843–3067. ISSN: 0034-4885. DOI: 10.1088/0034-4885/69/11/R01.

[4] Gordon L. Kane. "Supersymmetry: What? Why? When?" In: *Contemporary Physics* 41 (6 2000). DOI: 10.1080/00107510010001644.

[5] Stephen P. Martin. "A Supersymmetry Primer". In: (Sept. 1997). DOI: 10.1142/9789812839657_0001.

[6] Csaba Csaki. "The Minimal Supersymmetric Standard Model (MSSM)". In: (June 1996). DOI: 10.1142/S021773239600062X.

[7] G. F. Giudice and A. Romanino. "Split Supersymmetry". In: (June 2004). DOI: 10.1016/j.nuclphysb.2004.11.048.

[8] JoAnne L. Hewett et al. "Signatures of long-lived gluinos in split supersymmetry". In: (Aug. 2004). DOI: 10.1088/1126-6708/2004/09/070.

[9] S. Chatrchyan et al. "The CMS Experiment at the CERN LHC". In: *JINST* 3 (2008), S08004. DOI: 10.1088/1748-0221/3/08/S08004.

[10] K. Aamodt et al. "The ALICE experiment at the CERN LHC". In: *JINST* 3 (2008), S08002. DOI: 10.1088/1748-0221/3/08/S08002.

[11] A. Augusto Alves Jr. et al. "The LHCb Detector at the LHC". In: *JINST* 3 (2008), S08005. DOI: 10.1088/1748-0221/3/08/S08005.

[12] *ATLAS detector and physics performance: Technical Design Report, 1*. Technical design report. ATLAS. Geneva: CERN, 1999.

[13] "The ATLAS Experiment at the CERN Large Hadron Collider". In: *JINST* 3 (2008), S08003. 437 p. DOI: 10.1088/1748-0221/3/08/S08003.

[14] Gordon Kane and Aaron Pierce. *Perspectives on LHC Physics*. WORLD SCIENTIFIC, June 2008. Chap. 3, p. 30. ISBN: 978-981-277-975-5. DOI: 10.1142/6686.

[15] ATLAS Collaboration. "Search for non-pointing and delayed photons in the diphoton and missing transverse momentum final state in 8 TeV pp collisions at the LHC using the ATLAS detector". In: (Sept. 2014). DOI: 10.1103/PhysRevD.90.112005.

[16] The ATLAS collaboration. "Operation of the ATLAS trigger system in Run 2". In: *Journal of Instrumentation* 15 (10 Oct. 2020), P10004–P10004. ISSN: 1748-0221. DOI: 10.1088/1748-0221/15/10/P10004.

[17] Martin Rybar. "The ATLAS Run-2 Trigger Menu". In: (2019). URL: https://cds.cern.ch/record/2677532.

[18] Matteo Cacciari, Gavin P Salam, and Gregory Soyez. "The anti-k_t jet clustering algorithm". In: *Journal of High Energy Physics* 2008.04 (2008), pp. 063–063. DOI: 10.1088/1126-6708/2008/04/063. URL: https://doi.org/10.1088/1126-6708/2008/04/063.

[19] ATLAS Collaboration. "Performance of the ATLAS trigger system in 2015". In: *The European Physical Journal C* 77.5 (2017). DOI: 10.1140/epjc/s10052-017-4852-3. URL: https://doi.org/10.1140/epjc/s10052-017-4852-3.

[20] *Trigger menu in 2018*. Tech. rep. CERN, 2019. URL: https://cds.cern.ch/record/2693402.

[21] Torbjörn Sjöstrand *et al.* "An Introduction to PYTHIA 8.2". In: (Oct. 2014). DOI: 10.1016/j.cpc.2015.01.024.

[22] Johannes Bellm *et al.* "Herwig 7.0 / Herwig++ 3.0 Release Note". In: (Dec. 2015). DOI: 10.1140/epjc/s10052-016-4018-8.

[23] S. Agostinelli *et al.* "Geant4—a simulation toolkit". In: *Nuclear Instruments and Methods in Physics Research Section A: Accelerators, Spectrometers, Detectors and Associated Equipment* 506.3 (2003), pp. 250–303. ISSN: 0168-9002. DOI: https://doi.org/10.1016/S0168-9002(03)01368-8. URL: https://www.sciencedirect.com/science/article/pii/S0168900203013688.

[24] Zachary Marshall. "Simulation of Pile-up in the ATLAS Experiment". In: *Journal of Physics: Conference Series* 513 (2 June 2014), p. 022024. ISSN: 1742-6588. DOI: 10.1088/1742-6596/513/2/022024.

[25] https://atlassoftwaredocs.web.cern.ch/.

[26] "Collider Searches for LLPs Beyond the Standard Model". In: (Oct. 2018). DOI: 10.1016/j.ppnp.2019.02.006.

[27] Heather Russell. *An experimental introduction to long ... - indico.cern.ch*. https://indico.cern.ch/event/607314/contributions/2542309/attachments/1447873/2231444/20170424_LLPs.pdf.

[28] *Search for long-lived charginos based on a disappearing-track signature using 136 fb^{-1} of pp collisions at $\sqrt{s}$ = 13 TeV with the ATLAS detector*. Tech. rep. Geneva: CERN, 2021. URL: https://cds.cern.ch/record/2759676.

[29] "Search for long-lived, massive particles in events with displaced vertices and missing transverse momentum in $\sqrt{\{s\}}$ = 13 TeV pp collisions with the ATLAS detector". In: (Oct. 2017). URL: http://arxiv.org/abs/1710.04901 http://dx.doi.org/10.1103/PhysRevD.97.052012.

[30] ATLAS Collaboration. "Search for long-lived neutral particles in pp collisions at $\sqrt{\{s\}}$ = 13 TeV that decay into displaced hadronic jets in the ATLAS calorimeter". In: (Feb. 2019). DOI: 10.1140/epjc/s10052-019-6962-6.

[31] Christian Ohm. "Searches for exotic stable massive particles with the ATLAS experiment". Presented 04 Nov 2011. 2011. URL: cds.cern.ch/record/1397376.

[32] "Search for heavy charged long-lived particles in the ATLAS detector in 36.1 fb^{-1} of proton-proton collision data at $\sqrt{s} = 13$ TeV". In: *Phys. Rev. D* 99 (9 2019). DOI: 10.1103/PhysRevD.99.092007. URL: link.aps.org/doi/10.1103/PhysRevD.99.092007.

[33] "Search for magnetic monopoles and stable particles with high electric charges in 8 TeV pp collisions with the ATLAS detector". In: *Phys. Rev. D* 93 (5 2016). DOI: 10.1103/PhysRevD.93.052009. URL: link.aps.org/doi/10.1103/PhysRevD.93.052009.

[34] *Performance of the reconstruction of large impact parameter tracks in the ATLAS inner detector*. Tech. rep. Geneva: CERN, 2017. URL: https://cds.cern.ch/record/2275635.

[35] ATLAS Collaboration. "Search for long-lived, massive particles in events with displaced vertices and missing transverse momentum in $\sqrt{\{s\}}$ = 13 TeV pp collisions with the ATLAS detector". In: (Oct. 2017). DOI: 10.1103/PhysRevD.97.052012.

[36] Wen Han Chiu et al. "Jet Timing". In: (2021). DOI: 10.1007/JHEP01(2022)014.

[37] https://acode-browser1.usatlas.bnl.gov/lxr/source/athena/Reconstruction/Jet/JetUtils/Root/JetCaloQualityUtils.cxx#0232.

[38] CMS Collaboration. "Search for long-lived particles using nonprompt jets and missing transverse momentum with proton-proton collisions at $\sqrt{\{s\}} = 13$ TeV". In: (June 2019). DOI: 10.1016/j.physletb.2019.134876.

[39] Florian Beaudette. "The CMS Particle Flow Algorithm". In: (2014). DOI: 10.48550/ARXIV.1401.8155. URL: https://arxiv.org/abs/1401.8155.

[40] https://its.cern.ch/jira/browse/ATLMCPROD-8099.

[41] https://its.cern.ch/jira/browse/ATLMCPROD-6041.

[42] https://twiki.cern.ch/twiki/pub/AtlasPublic/TriggerOperationPublicResults/menuTable.png.

[43] https://twiki.cern.ch/twiki/bin/view/AtlasPublic/TriggerOperationPublicResults#Trigger_rates_and_bandwidth_for.

[44] https://acode-browser1.usatlas.bnl.gov/lxr/source/athena/Reconstruction/Jet/JetRecConfig/python/StandardJetMods.py#0093.

[45] https://acode-browser1.usatlas.bnl.gov/lxr/source/athena/Trigger/TriggerCommon/TriggerMenuMT/python/HLT/Jet/JetRecoSequences.py#0198.

[46] https://acode-browser1.usatlas.bnl.gov/lxr/source/athena/Trigger/TriggerCommon/TrigEDMConfig/python/TriggerEDMRun3.py#0075.

[47] https://acode-browser1.usatlas.bnl.gov/lxr/source/athena/Trigger/TrigSteer/TrigOutputHandling/TrigOutputHandling/TriggerEDMAuxAccessors.h#0142.

[48] https://gitlab.cern.ch/atlas/athena/-/merge_requests/49223.

[49] Anna Sfyrla. *From raw data to physics results - (2/3)*. URL: https://indi.to/2r6wr.

[50] https://its.cern.ch/jira/browse/ATR-25424.

[51] ATLAS Collaboration. *Expression of Interest: A High-Granularity Timing Detector for ATLAS Phase-2 Upgrade*. Tech. rep. Geneva: CERN, 2017. URL: https://cds.cern.ch/record/2290829.